Department of Environment Systems
Graduate School of Frontier Sciences
The University of Tokyo

2019
Master's Thesis

Evaluation of effects of retro-reflective window film on the outdoor thermal environment and cooling energy consumption using an urban canopy model considering the specular and retro reflections of solar radiation
（鏡面反射・再帰反射を考慮した都市キャノピーモデルを用いた再帰反射フィルムによる屋外熱環境の改善効果及び省エネ効果の評価）

Submitted July 26, 2019

Adviser: Associate Professor Tomohiko Ihara

Ruyue Fang

To my parents, Xuebin Fang and Huiqing Wang,
For their love and support.

ACKNOWLEDGMENTS

First, I would like to express my deep gratitude to Professor Ihara for his mentoring, support, and encouragement as my advisor. The door to his office was always open whenever I ran into a trouble spot or had a question about my research. He always steered me in the right direction whenever he thought I needed it. And more importantly, his tireless efforts and rigorous attitude towards scholarship influenced and inspired me throughout my graduate study.

Besides my advisor, I would like to thank Yamagushi san. This research would not have been completed successfully without his help. And a special thanks to Harima san from Dexerials Corporation for providing me with crucial data. In addition, I am grateful to Dr. Hashimoto, Kuwayama san, Nishimoto san and Liu san. I benefitted a lot from their patient guidance and valuable suggestion on my research. I would also like to thank the former and current members of Ihara Lab for creating such a superior environment for doing research and for all the fun we have had in the last two and a half years.

My sincere thanks also goes to my best friend, Menglan Wu who I can share all the joys and sorrows of my life with no matter how far apart we are. And to Xi Liu: for filling my life with happiness and supporting me consistently since I first came to Japan. So lucky and thankful to have you in my life.

I am deeply grateful to my boyfriend, Chentao Ye for always being the person I could turn to during those dark and desperate times of the past three years, and for enlightening me on how to establish the computational model of specular reflection which is the most important part of my research. Thank you so much, maomao.

And finally, to my dear parents, Xuebin Fang and Huiqing Wang: thank you for the unconditional trust and support throughout my years of study.

TABLE OF CONTENTS

LIST OF TABLES

LIST OF FIGURES

CHARPTER 1. INTRODUCTION

1.1 Background

Along with the growing global warming, a rise in the temperature has been observed. As showed in Figure 1.1, from 1990 to 2010, the annual average temperature has gone up by 3 ℃ in Tokyo, 1.3℃ in Japan, and the global average temperature also increased by 0.9℃. According to the latest report of Intergovernmental Panel on Climate Change (IPCC, 2013), during 21st century, the global surface temperature will continually increase by 0.3 to 4.8 °C, depending on the rate of future greenhouse gas emissions and its effect on the climate.

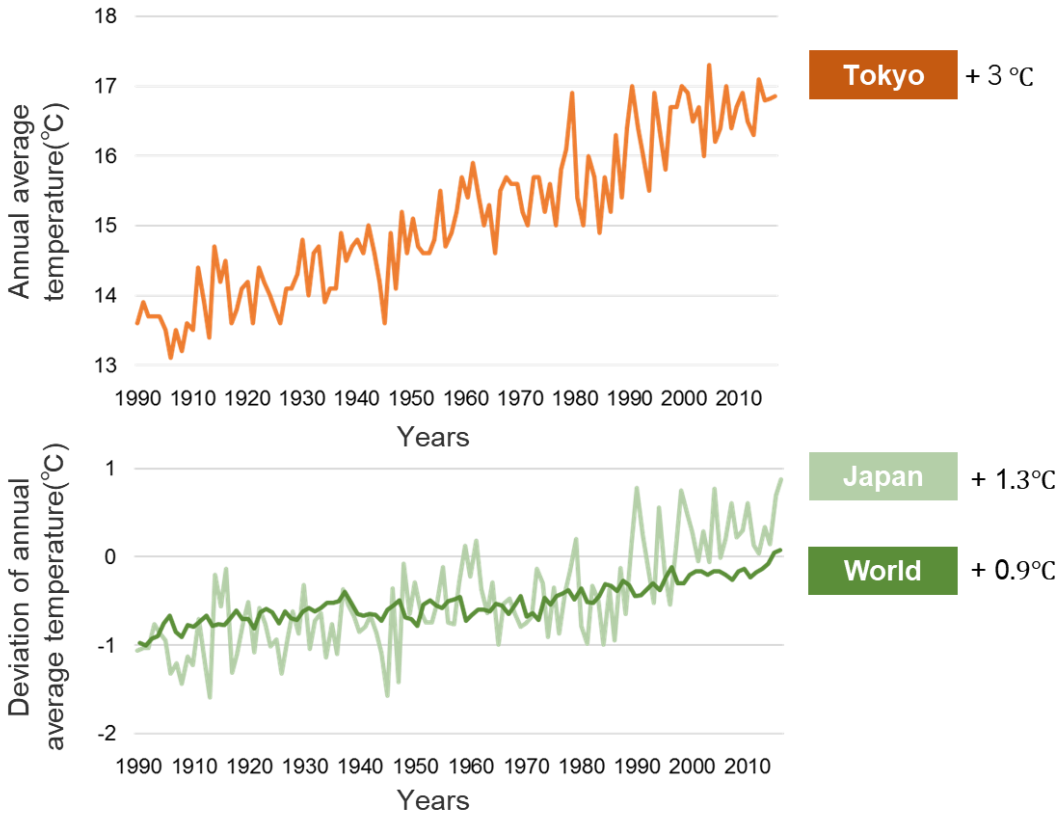

Figure 1.1. Variation of annual average temperature from 1990 to 2010 (Japan Meteorological Agency)

The urban heat island (UHI) effect, defined as a temperature rise in urban areas compared to the surrounding rural areas attributed to human activities, has a negative impact on the cooling energy demand, urban thermal environment and thermal comfort of open space, especially in summer days. The cause of the heat island effect is complicated. Firstly, due to the increasing coverage rate of asphalt and concrete with a high absorptance, the solar radiation incident on its surface are absorbed than natural surfaces (Doulos L, 2004). What's

more, the dense construction increases the interreflection between the buildings, which further intensify the absorption of the solar radiation. Besides, the urban surface roughness decreases the wind velocity, leading to a decrease in the heat removal from urban canopy by thermal convection. Another important factor is the anthropogenic heat to the atmosphere, such as the waste heat emitted from vehicles and air-conditioning (Sailor DJ, 2011). Figure 1.2 shows the temperature rise caused by the urbanization. In the highly urbanized area, the UHI effect is more significant.

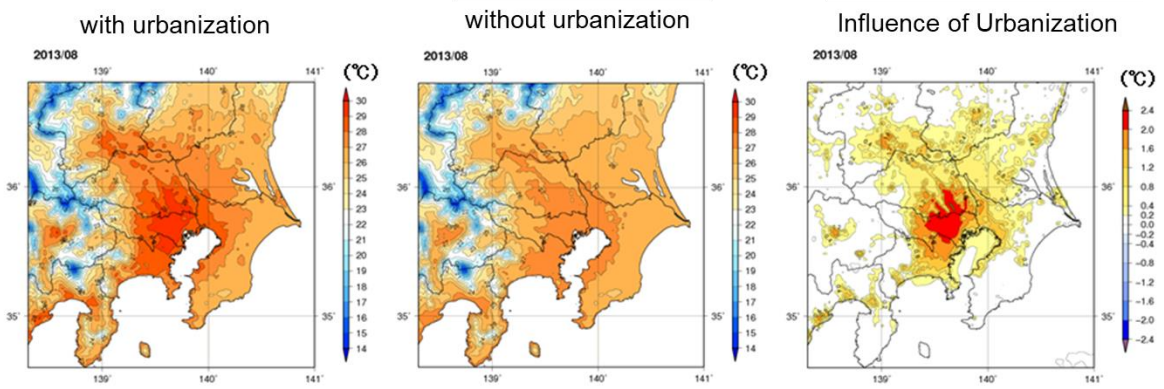

Figure 1.2. Change of the temperature due to the urbanization in Kanto district, August 2013 (Japan Meteorological Agency, 2013)

UHI contributes a lot to the rapidly growing building energy demand, which will be further intensified in summer days. Nearly 40% of the total energy is consumed by the building sector every year (Santamouris M et al, 2001). Being deeply affected by the air temperature, the building energy consumption increases by 10 % for a 2 K daily maximum UHI effect (Bueno B et al, 2012). What' more, as a feedback, the rise in building energy consumption will result in the increase of waste heat generated from the use of air-conditioning and further exacerbate the UHI. The effective energy-saving countermeasures are urgently needed.

Recently, the buildings with glass curtain wall emerge in a large number in the central business district of a city. With the increasing window to wall ratio of office buildings (Kim et al, 2009), the heat shading window films (HSF), which has a low transmittance of heat rays, is spreading with the purpose of reducing the energy consumption of air conditioning in summer. However, the increase of the specularly reflected solar radiation from its surface will further degrade the thermal environment in outdoor spaces instead (Yoshida, 2018). The central business district of Tokyo has a high heat disorder risk (Ohashi, 2016) due to its great daytime population. Therefore, the deterioration of the thermal environment in this area need to be taken seriously.

In order to solve this problem, the retro-reflective film (RRF), which allows to reflect the solar radiation back in the same direction of the incident radiation, has been recently proposed as an innovative solution for suppressing the degradation of the outdoor thermal environment caused by HSF, and in the meanwhile reducing building energy demand for cooling.

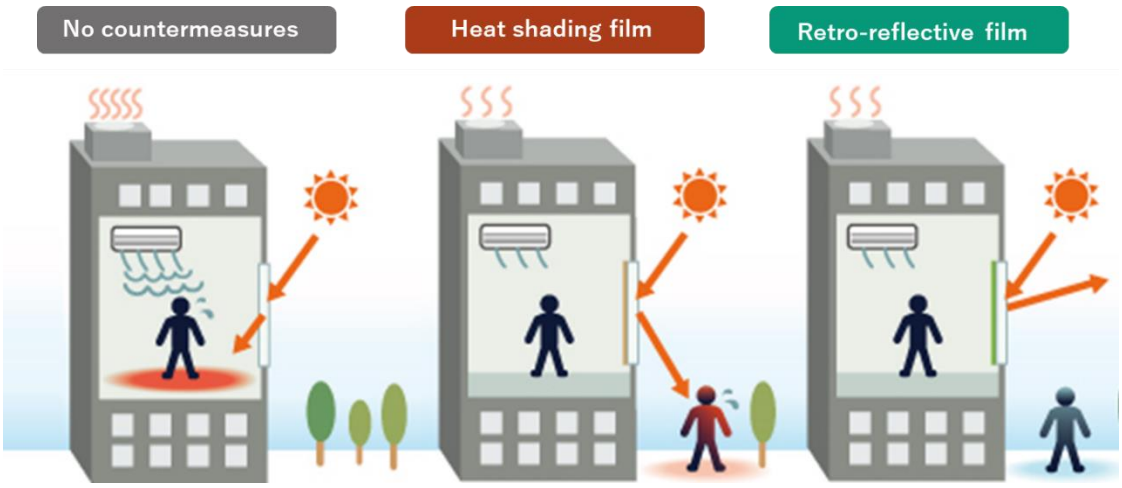

Figure 1.3. Impact of window films on the indoor and outdoor environment.

1.2 Retro-reflective window film

1.2.1 Mechanisms of the retro-reflection

Retro-reflection is a reflection phenomenon that the reflected lights go back to the same direction of incidence. The martials with retro-reflective properties have been widely used in our daily life, such as the road and traffic signs. When the headlights of a car illuminate a retro-reflective surface, the light will be reflected towards the car, so that the driver can read the information on it. As illustrated in Figure 1.4, there are two main mechanisms of retro reflection from a surface: the glass-bead type and the prism type. The former one reflects the light back by focusing the lights on an arc surface and the later one is though the multiple.

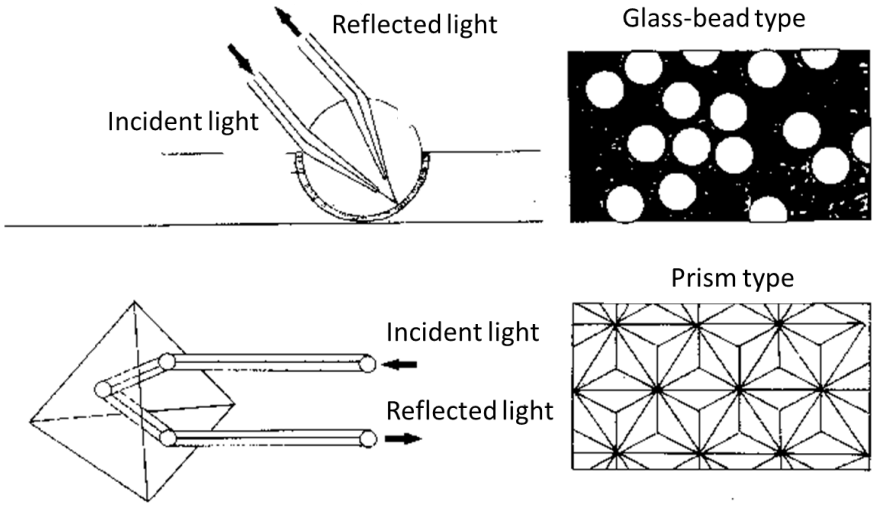

Figure 1.4. Mechanisms of the retro-reflection (Sakai et al, 2011)

The retro-reflective window film used in this study is produced by Dexerials Corporation. It processes a pyramid shape embedded microstructure as shown in Figure 1.5. The near-infrared ray is reflected several times between the V-shaped surfaces, and then returns to the sky. In addition to its retro-reflective properties, the window films can also block about 70% of near infrared rays and 99.5% of UV light out and allow about 67% of visible light pass through the window in the meanwhile (Dexerials Corporation HP, 2019).

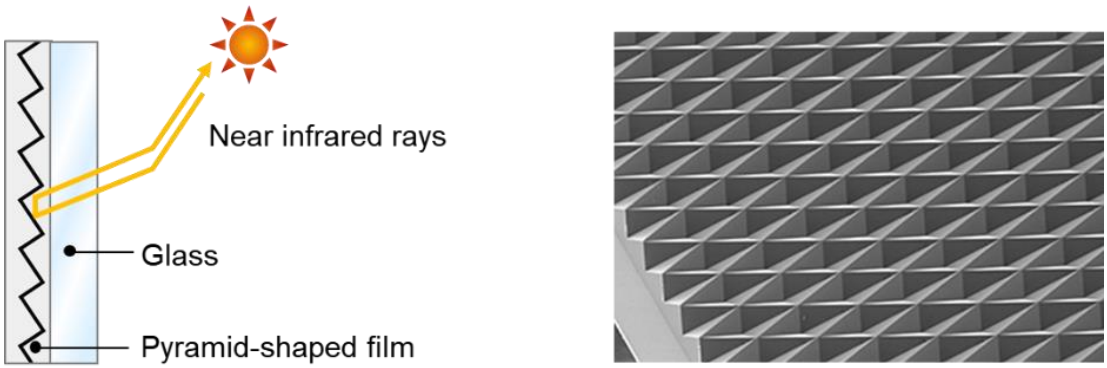

Figure 1.5 Mechanisms of retro-reflective film and enlarged photo of its surface (Dexerials Corporation HP, 2019)

1.2.2 Mechanism of thermal environment improvement

Thermal comfort is affected by many factors, including the air temperature, radiant environment, wind velocity, and relative humidity, and clothing and metabolism of a man (Taleghani M et al, 2013). Several studies have shown that radiation plays a significant role on thermal comfort. (Taleghani M et al, 2014; Taleghani M et al, 2015)

The radiation incident on the pedestrian' body surface has two forms. The first one is shortwave radiation, including the direct solar radiation, diffuse solar radiation, and reflected solar radiation from the surfaces that surround the pedestrian in the built environment. The second one is longwave radiation, including longwave atmospheric counter radiation and longwave emission from building and ground surfaces. With the installation of RRF, the reflected shortwave radiation to the street spaces decreases first. Due to its reduction, the temperature rise in the ground and wall surfaces is suppressed subsequently, leading to the reduction of longwave re-emission from ground and wall surfaces. At approximately noon, the reflected solar radiation and longwave re-emission from ground and wall accounts for about 50% of total radiation entering to the street spaces (Ministry of the Environment Government of Japan, 2013). Therefore, the retro reflective film has a great potential for improving the thermal environment in street spaces.

1.3 Objectives

As mentioned above, the ongoing global warming and urban heat islands have resulted in a significant increase in the cooling energy consumption, and the degeneration of urban thermal environment, especially in the central business district with a high density of population and buildings.

Recently, with the increasing window to wall ratio in the office building, the heat shading window film is spreading with the purpose of reducing the energy consumption of air conditioning in summer. However, the increase of the specular reflected solar radiation from its surface, which is caused by the increase of the reflectivity, will degrades the thermal environment in outdoor spaces instead (Yoshida et al, 2018). As its solution, the retro-reflective film, which can reflect the solar radiation back in the same direction of the incident radiation, has both the improvement effect on the outdoor thermal environment and energy-saving effect. But the feasibility of installing the retro-reflective films to the exterior wall of buildings in the urban block scale has not been assessed yet.

What's more, for evaluating the effects on the outdoor thermal environment and on the cooling energy consumption simultaneously, a canopy model coupled with a building energy simulation model is necessary. However, most of them consider the window as a perfectly diffuse surface. For this reason, it is very hard to simulate the directional optical properties of retro-reflective films.

Therefore, the main objective of this study is to develop a new computational method of radiation heat transfer considering the specular and retro reflections of solar radiation in the CM-BEM model (Kikegawa et al, 2003) first and then apply it evaluate the impact of retro-reflective window films on the summer outdoor thermal environment and cooling energy consumption in the 23 wards of Tokyo.

CHAPTER 2. NUMERICAL SIMULATION SYSTEM (WRF-CM-BEM)

The numerical simulation system that can explore the interaction between outdoor thermal conditions and energy consumption of air conditioning in buildings (Kikegawa et al, 2003) was utilized and improved in this study. And the system has been coupled with the sub-model for the evaluation of thermal comfort in outdoor environment (Ohashi et al, 2014).

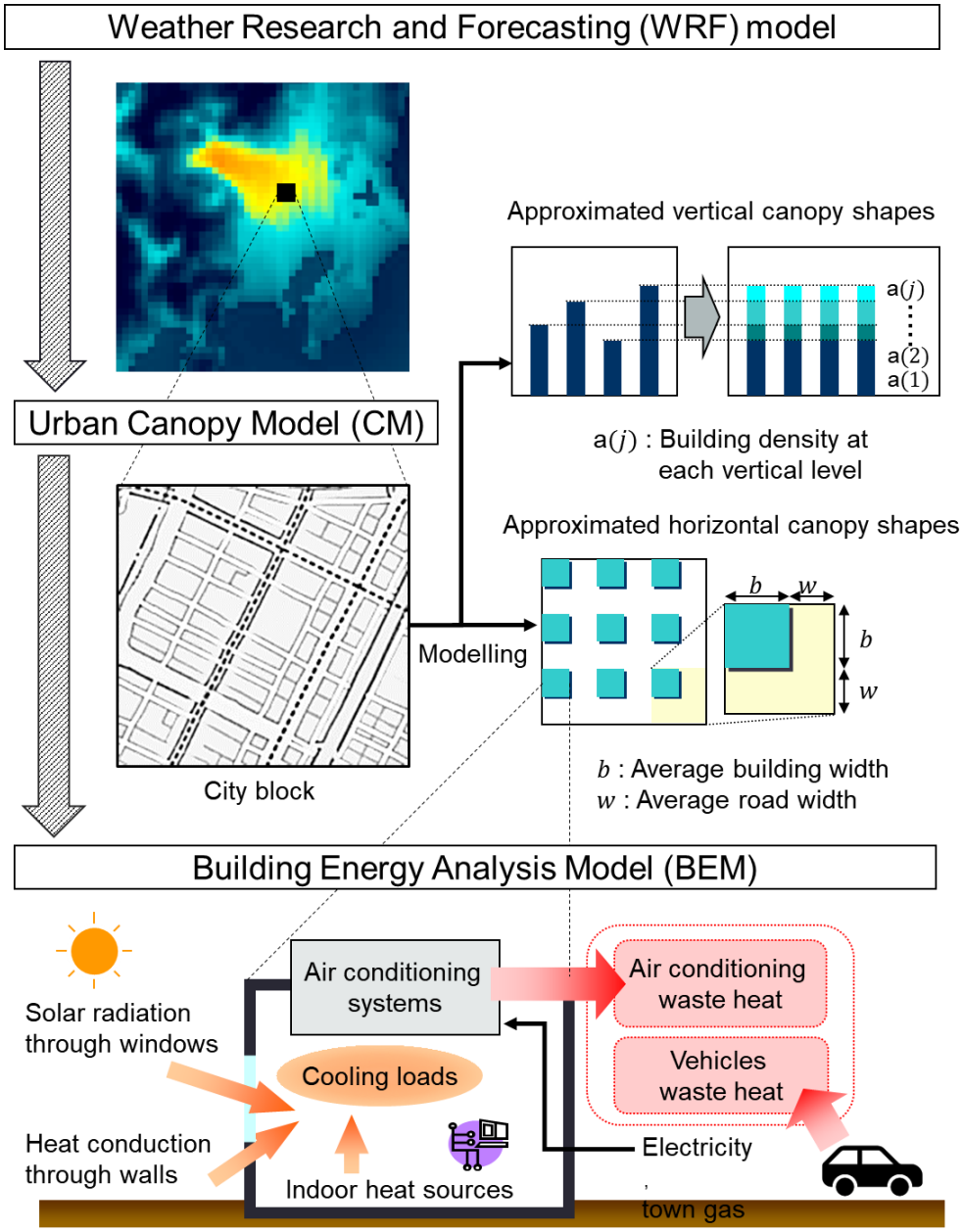

Figure 2.1 Composition of the simulation models (WRF-CM-BEM)

2.1 Framework of the simulation system

Figure 2.1 shows the composition of the simulation system (Kikegawa et al, 2003). The simulation system consists of three sub-models: a mesoscale meteorological model, an urban canopy model, and a building energy simulation model. The Weather Research and Forecasting (WRF) model, which is developed by the National Center for Atmospheric Research (NCAR) was used for calculating atmospheric motion. However, considering the large mesh size of this model, it is difficult to take account of the impact of the urban canopies on the surface boundary layer over cities. For this reason, a multi-layer urban canopy model (CM) was adopted for the city-block-scale meteorological forecast. What's more, in order to consider the architectural responses of air-conditioning energy consumption and its consequent waste heat emitted into the urban atmosphere, a building energy analysis model (BEM) was incorporated.

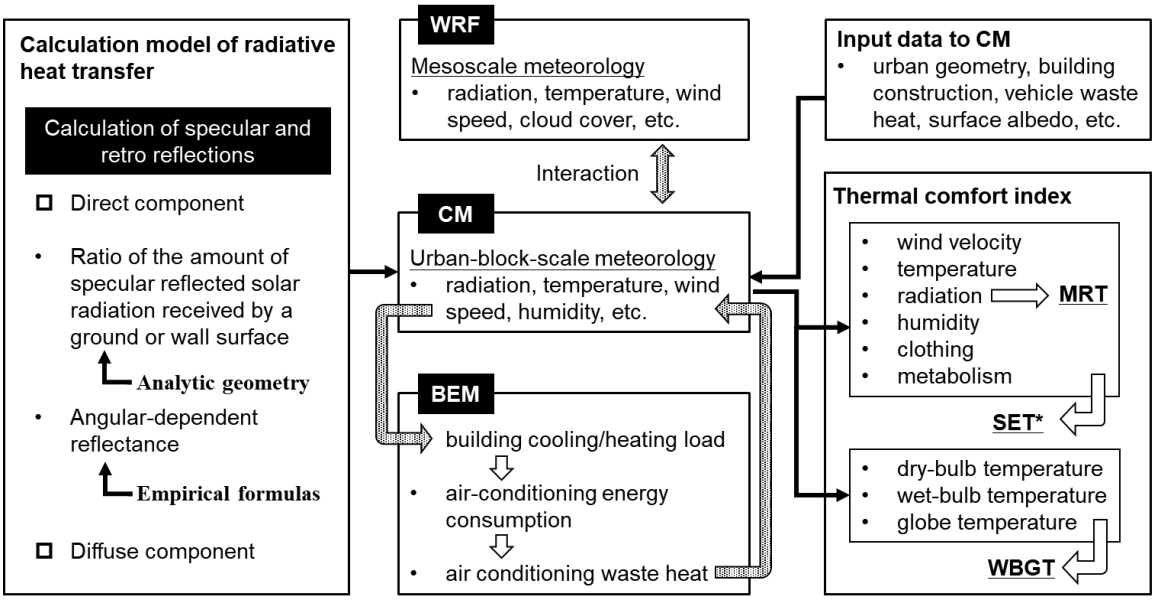

Figure 2.2 Computational flow of the simulation models (WRF-CM-BEM) coupled with calculation model of directional reflection of solar radiation

Figure 2.2 shows the calculation flow of the simulation system. Initial conditions and the upper boundary conditions of CM atmosphere are obtained from WRF outputs. In CM, the meteorological conditions around buildings are simulated. For evaluating the thermal comfort level of pedestrians in outdoor spaces, the thermal comfort indices, such as mean radiant temperature (MRT), Wet Bulb Globe Temperature (WBGT) and new standard effective temperature (SET*) are calculated based on the results obtained in CM. BEM calculates the cooling load in the buildings (Q_C) and the energy consumption of air

conditioning (E_C). E_C is determined by the coefficient of performance (COP) of the air conditioners. The total amount of air conditioning waste heat (Q_A) to the CM atmosphere is equivalent to the sum of Q_C and E_C. And for the calculation of radiative heat transfer in CM, it will be described in Chapter 4.

2.2 Details of WRF, CM and BEM models

The following equations for the dramatic calculation of the atmospheric temperature in the CM and the cooling energy consumption in BEM

WRF is based on fluid dynamics equations incorporating fully compressible fluids and non-hydrostatic equilibrium (Ohashi et al, 2016). Its horizontal grid spacing is 5km×5km in this study.

CM is a vertical one-dimensional model. which can compute the temporal variations of air temperature, humidity and wind velocity in the urban canopy. The complicated radiation processes in the building environment was also considered. The larger scale meteorological influences from outside of the urban canopy were introduced to CM by a double direction connection with WRF. The urban block are sub grids of the WRF grids with the size of 0.5km×0.5km. In each grid, buildings stand on a lattice array as shown in Fig.1. The horizontal shape of block is described using two parameters: average width of building, indicated with b, and the average road with, indicated with w. For the vertical direction, building heights are represented through building density at each vertical level in the urban canopy, indicated with $a(j)$.

For calculating the air temperature in CM, the following equation (Kikegawa et al, 2003) was used.

$$C_P\rho\frac{\partial\theta}{\partial t} = C_P\rho\frac{1}{m}\frac{\partial}{\partial j}\left(K_h m\frac{\partial\theta}{\partial j}\right) - C_P\rho(\alpha V_M)\theta_M + Q_A + Q_V$$

Where, $\theta\ (K)$ indicates the air temperature in the urban canopy. C_p ($\mathrm{Jkg^{-1}\,K^{-1}}$) and ρ ($\mathrm{kgm^{-3}}$) denote specific heat of air and air density respectively. On the right side of the equation, the second term represents the cooling/heating rate due to the larger-scale atmospheric advection (such as land and sea breeze) outside the urban canopy. It is inputted from WRF considering the wind velocity attenuation in the urban canopy. Q_A indicates the air-conditioning waste heat calculated by BEM. Its calculation method was described hereafter. And Q_V indicates the vehicle waste heat. Moreover, K_h ($\mathrm{m^2\,s^{-1}}$) denotes the vertical turbulent diffusion coefficient of sensible heat. $m\ (-)$ represents the effective volume ratio of the air in the urban canopy consisting of the atmosphere and buildings. V_M and θ_M denotes the wind velocity and air temperature respectively, which both are computed by WRF. And $\alpha\ (-)$ denotes the ratio of the CM wind velocity against V_M.

BEM calculates the heat exchange between buildings and the atmosphere in CM. The building in the urban block is treated as a box and divided into three types: office and commercial buildings, apartment and detached house. Each type has different building envelops and air-conditioning operating schedules. The input parameters are the solar radiation transmitted from windows, conductive heat through walls, convective heat flow, and internal heat generated by lightings, machines, and humans. The main output parameter is the waste heat emitted from air conditioners. The cooling loads in the buildings are calculated from the sensible and the latent heat components, respectively.

The total amount of sensible heat load H_{in} (W) and latent heat load H_{in} (W) are calculated using the following equations (Kikegawa et al, 2003).

$$H_{in} = \sum_{m} A_m h_{cm}(T_{wm} - T_r) + \sum_{n} A_n \eta_n S_n + (1-\beta) C_p \rho V_a (T_a - T_r) + A_f q E + A_f P_{\varphi_P} q_{hs}$$

$$E_{in} = (1-\beta) \iota \rho V_a (T_a - T_r) + A_f q E + A_f P_{\varphi_P} q_{hl}$$

Where, the subscripts i and j denotes the elements of the indoor surfaces of walls and windows respectively. In the first equation, the right-hand terms represent components of the sensible heat load. The first term represents its heat exchange between walls and indoor air, and the second term represents the transmission of the solar insolation through the windows. The third term corresponds to the sensible heat exchange through ventilation. The fourth and last term indicates the internal sensible heat generation from the equipment and occupants, respectively. In the second equation, the first right hand term of stands for the water vapor intrusion through ventilation and the second right-hand term indicates the evaporation from occupants.

In addition, A_m (m^2) and A_n (m^2) denote the areas of the wall and window surface respectively. h_{cm} ($\mathrm{Wm^{-2}\,K^{-1}}$) denotes the convective heat transfer coefficient. T_{wm} (K) denotes indoor surface temperature of the walls. T_r (K) denotes indoor air temperature, which is fixed to the air-conditioning target values. T_a (K) denotes outdoor air temperature**.** η_n $(-)$ denotes insolation transmittance through the windows. S_n ($\mathrm{Wm^{-2}}$) denotes solar insolation on the windows**.** β $(-)$ denotes thermal efficiency of the total heat exchanger. C_p ($\mathrm{Jkg^{-1}\,K^{-1}}$) denotes specific heat of air. ρ ($\mathrm{kgm^{-3}}$) denotes air density. V_a ($\mathrm{m^3\,s^{-1}}$) denotes total ventilation rate in the building.A_f (m^2) denotes air-conditioned floor area. q_E ($\mathrm{Wm^{-2}}$) denotes sensible heat gain from equipment per floor area. P ($\mathrm{person\ m^{-2}}$) denotes peak number of occupants per floor area. φ_p $(-)$ denotes ratio of hourly occupants to P. q_{hs}

($\mathrm{W\,person^{-1}}$) denotes sensible heat generation from the occupants. q_{hl} ($\mathrm{W\,person^{-1}}$) denotes latent heat generation from the occupants. ι ($\mathrm{kg^{-1}}$) denotes latent heat of evaporation. q_{Va} ($\mathrm{kg\,kg^{-1}}$) denotes specific humidity of the outdoor air. q_{Vr} ($\mathrm{kg\,kg^{-1}}$) denotes specific humidity of the room air.

Here, outdoor air temperature T_a, solar insolation on the windows S_n and specific humidity of the outdoor air q_{Va} are dynamically computed by CM and inputted to BEM. For the full air-conditioning occasion, indoor air temperature T_r and indoor specific humidity q_{Vr} are fixed to the air-conditioning target values. Meanwhile, the heat budget on the outdoor surface of the wall was also considered in the CM.

The following equations (Kikegawa et al, 2003) are used for the calculation of the cooling load Q_c (W) and cooling energy consumption of air-conditioning E_C (W).

$$Q_c = H_{out} + E_{out}, H_{out} = \varphi_P H_{in},\ E_{out} = \varphi_P E_{in}$$

$$E_C = \frac{Q_c}{COP}$$

Where H_{out} and E_{out} indicate the sensible and latent heat pumped out from the building for cooling, respectively. When the air-conditioning is fully operating, φ_P is equal to 1. COP represents the coefficient of performance of the air conditioners.

The connection between CM and BEM is bi-directional. The waste heat caused by the energy consumption of the air conditioning (Q_A) is equivalent to the sum of Q_C and E_C as showed in the following equation (Kikegawa et al, 2003).

$$Q_A = E_C + Q_C$$

2.3 Thermal index calculation

The commonly used thermal indices, Mean Radiant Temperature (MRT), Wet Bulb Globe Temperature (WBGT) were calculated based on the meteorological outputs from CM. For simplicity, the human body was assumed to be a sphere in calculation.

The MRT sums up all short and long wave radiation fluxes in the ambient environment to which the human body is exposed. It is calculated using the heat budget equation as follows:

$$4\pi r^2 \varepsilon \sigma (MRT + 273.15)^4 = \alpha\left[\pi r^2 R_{dir} + 2\pi r^2 \left(R_{diff} + R_{ref}\right)\right] + 2\pi r^2 \varepsilon (L_d + L_u)$$

Where R_{dir} (W) and R_{diff} (W) denote the direct and diffuse solar radiations from the sky, respectively; R_{ref} (W) indicates the solar radiation reflected from the ground and building surfaces; L_d (W) and L_u (W) are longwave radiation from the atmosphere and ground and building surfaces; r (0.15) is radius of assumed sphere the ε (0.97) and α (0.7) are the emissivity and absorptivity of the human body; σ denotes the Stefan–Boltzmann constant.

The outdoor WBGT is calculated from dry bulb temperature, wet bulb temperature and globe temperature with different weights as showed in the following equation.

$$\mathrm{WBGT} = 0.1T_d + 0.7T_w + 0.2T_g$$

where T_d (℃), T_w (℃), and T_g (℃) denote the dry-bulb temperature, natural wet-bulb temperature and globe temperature, respectively. T_g is estimated from the heat budget equation for a modeled globe thermometer and the influence of wind speed is also considered. The details of calculation can be seen in (Ohashi et al, 2016)

2.4 Conclusions

In this chapter, the basic framework of simulation systems was described, followed by the calculation method of thermal indices MRT and WBGT. The equations mentioned above are the fundamental equations for the dramatic calculation of the atmospheric temperature in the CM and the cooling energy consumption in BEM, with the consideration of the interaction between outdoor thermal conditions and cooling-energy demands of buildings.

The calculation of radiative heat transfers on the ground, roof and wall surfaces is also involved in CM. However, in this study, the method of radiative heat transfer calculation was improved to reproduce the specular and retro-reflective characteristics of reflected solar radiation from window surface. For the explicit interpretation of this newly developed method, it will be described individually in Chapter 3.

CHAPTER 3. DEVELOPMENT OF A CALCULATION MODEL OF RADIATIVE HEAT TRANSFER CONSIDERING SPECULAR AND RETRO REFLECTIONS OF SOLAR RADIATION

3.1 Definition of solar azimuth angle (α), elevation angle (β) and incidence angle (θ)

In the calculation of specular reflection of solar radiation, the solar incidence angle to a glass surface is one of the significant parameters to describe the direction of reflected solar beams and the variations of glass optical properties. It could be calculated by the solar azimuth angle and elevation angle.

The solar azimuth angle (α) is defined as the angle of the sun's rays measured in the horizontal plane clockwise from due north. And the solar elevation angle (β) is defined as the angle of sun's rays measured up from the horizontal plane. Figure 3.1 illustrates the definitions of α and β.

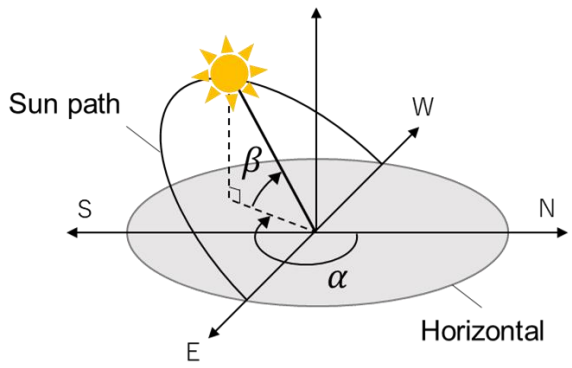

Figure 3.1. Definitions of the solar elevation angle (β) and azimuth angle (α)

To reproduce the optical properties of the glass which vary with the different incident angle of a light beam, the solar incidence angel was used in this model. The incidence angle (θ) is defined as the angle between the sun's rays and the normal line to the window surface ($\theta = 0°$ is normal to the window surface, while $\theta = 90°$ is tangential to the window surface). As only the sun azimuth and azimuth angles were calculated in the canopy model (CM), a method was developed to calculate the incidence angle. Figure 3.2 illustrates the relationship of solar elevation angle , azimuth angle and incidence angle on a south or north facing window surface.

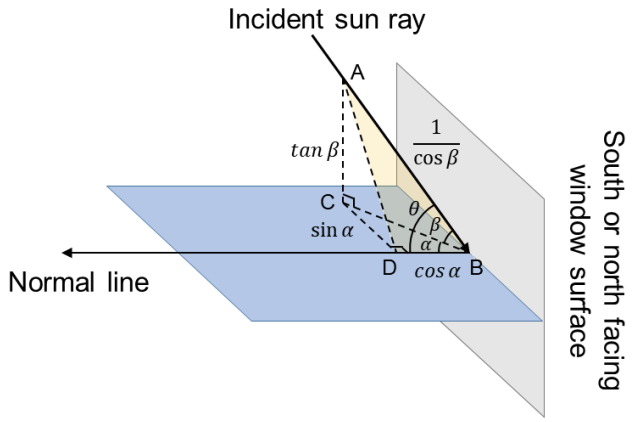

Figure 3.2. The relationship of solar elevation angle (β), azimuth angle (α) and incidence angle (θ) on a south or north facing window surface

If the length of BC side is assumed to be 1, the solar incidence angle (θ) is calculated using the cosine formula as follows.

For a south or north facing window surface,

$$\cos\theta = \frac{(\cos\alpha)^2 + (1/\cos\beta)^2 - (\sin\alpha)^2 - (\tan\beta)^2}{2 * |\cos\alpha| * |1/\cos\beta|}$$

For an east or west facing window surface,

$$\cos\theta = \frac{(\sin\alpha)^2 + (1/\cos\beta)^2 - (\cos\alpha)^2 - (\tan\beta)^2}{2 * |\sin\alpha| * |1/\cos\beta|}$$

3.2 Fundamental equations for radiative heat transfer calculation

In the canopy model (CM), which was mentioned in Chapter 2, the roof and wall surfaces were assumed to exist at each floor in the vertical direction of the urban canopy. The radiative heat transfer calculation on the road surface and each floor of the roof and wall surface were calculated respectively. The following equation shows the calculation of radiation gain on each surface.

$$I = \alpha\left(R_{dir} + R_{diff} + R_{ref}\right) + \varepsilon(L_d + L_u)$$

Where R_{dir} (W) and R_{diff} (W) denote the direct and diffuse solar radiations from the sky, respectively; R_{ref} (W) indicates the solar radiation reflected from the ground and building surfaces; L_d (W) and L_u (W) are longwave radiation from the atmosphere and ground and building surfaces; ε (0.97) and α (0.7) are the emissivity and absorptivity of the surface, respectively. The amount of R_{diff}, R_{dir}, L_d and L_u do not change whether the specular and retro reflection of solar radiation are considered or not.

In the previous models, the amount of reflected solar radiation from the adjunct window surfaces (wall surfaces), indicated with R_{ref_w}, was calculated by the following equation.

$$R_{ref\_w} = \sum\left(R_{dir\_j} + R_{diff\_j}\right) \cdot P_j \cdot \rho \cdot a(j) \cdot \mu$$

Where the subscripts j denotes the number of floors of adjunct building walls. $a(j)$ $(-)$ denotes the jth floor density, representing the building density at the vertical level ($a(5) = 0.5$ stands for half the buildings have the fifth floor). μ $(-)$ denotes the window to wall ratio calculated by dividing the building's total glazed (windows) area by its exterior envelope wall area and its values of each building floor are set to the same. R_{dir_j} (W) and R_{diff_j} (W) denotes the direct and diffuse solar radiation gains to the j floor window surface, respectively. P_j $(-)$ denotes the proportion of the amount of reflected solar radiation reaching the receiving surface to the total amount from window surface. And ρ $(-)$ is the reflectance of window with a constant value.

In the equation above, the direct and diffuse solar radiation could be calculated together since the window surface was assumed to be a perfect diffuse surface. However, after considering the specular and retro reflection of solar radiation, the reflected solar beams of direct component become directional while the reflect beams of diffuse component is still

nondirectional. Thus, in the new model, the calculation equation of R_{ref_w} was extended as follows:

$$R_{ref\_w} = \sum \left[R_{dir\_j} \cdot P_{d\_j} \cdot \rho_d(\theta) + R_{diff\_j} \cdot P_{df\_j} \cdot \rho_{df} \right] \cdot a(j) \cdot \mu$$

Where $P_{d\_j}\,(-)$ and $P_{df\_j}\,(-)$ denote the direct and diffuse component of P_j, respectively $\rho_s\ (-)$ indicates the reflectance of the window surface generated by diffuse solar radiation with a constant value while $\rho_d(\theta)\ (-)$ indicates the angular-dependent reflectance generated by direct solar beams.

It should be pointed out that the calculation was based on the premise of primary reflection.

The calculation method of P_{d_j} and P_{df_j} was described in section 3.3, followed by the $\rho_d(\theta)$ and ρ_s calculation in section 3.4.

3.3 Calculation of specular reflected solar radiation from window surface

In the previous studies, the anisotropic body of rotation of the normal distribution function (AND) model has been utilized to calculated directional solar reflection (Yoshida et al, 2018) and (Nakaohkubo et al, 2008). However, this method requires the large mesh numbers of each surface, which could not be implemented under the existing framework of CM model. And even if it is realized, it is at the expanse of the computation efficiency. Thus, the question remains how to calculate the specular reflection of solar radiation under the premise that the road surface, and roof and wall surfaces on each floor were treated as a whole, rather than divided into small grids.

In next section 3.3.1, a new method using analytic geometry was developed to calculate the value of P_{d_j} , which represent the proportion of the amount of reflected direct solar beams reaching the receiving surface to the total amount from window surface. And the computation of the proportion of diffuse component P_{df_j} was described in section 3.3.2

3.3.1 Specular reflection of direct component

As illustrated in Figure 3.3, the receiving surface was projected on the wall surfaces (where the windows distribute uniformly) of adjunct building along the opposite direction of reflected light. Based on the theorem that light travels in straight line, the reflected solar beams from the wall areas where the projection is located, could reach this receiving surface. Thus, the ratio of the projection area on jth floor to the jth floor wall area is equivalent to the value of P_{df_j} as showed in the following equation.

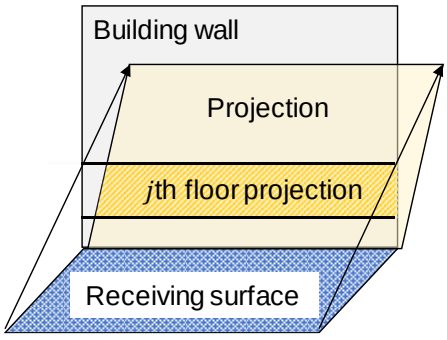

Figure 3.3. The projection of receiving surface on the adjunct building wall

$$P_{df\_j} = \frac{1}{A} S_j$$

Where A denotes the area of jth floor wall and S_j denotes the area of projection on jth floor.

Next, the calculation method of projection area S_j was introduced, taking the road surface between building walls as example. For the other receiving surfaces, the crossing road surface, roof surface and opposite wall surface, the calculating method is the same. The projections of each surface and their computational domain (only the reflected solar beams from the buildings in this domain was considered) were shown in Figure 3.4.

a. The projection of road surface between walls (front view)

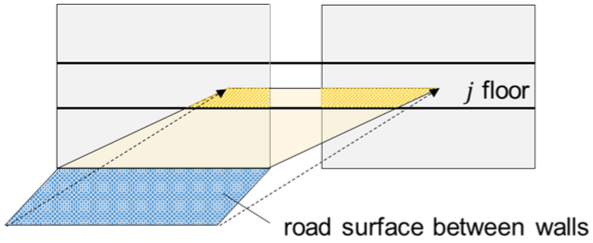

Computational Domain (top view)

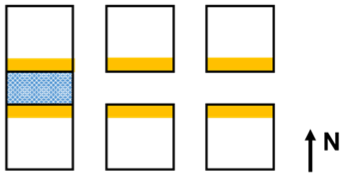

b. The projection of crossing road surface (front view)

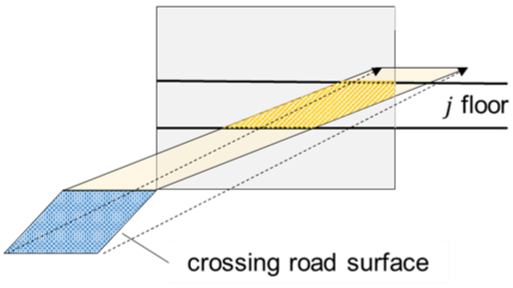

Computational Domain (top view)

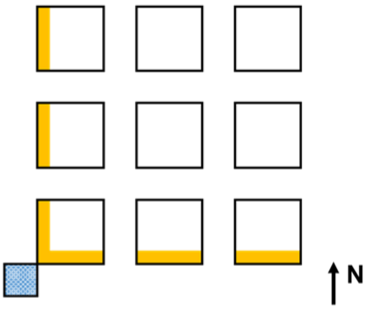

c. The projection of rooftop surface (front view)

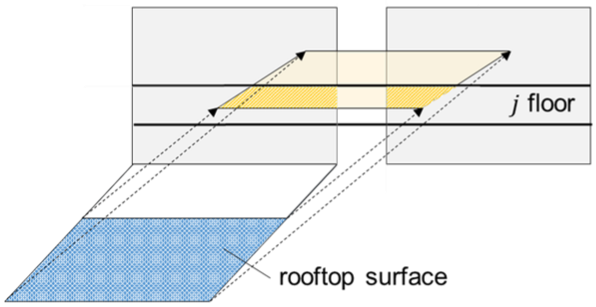

Computational Domain (top view)

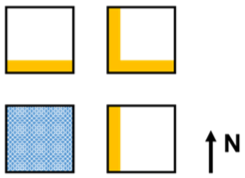

d. The projection of parallel wall surface (front view)

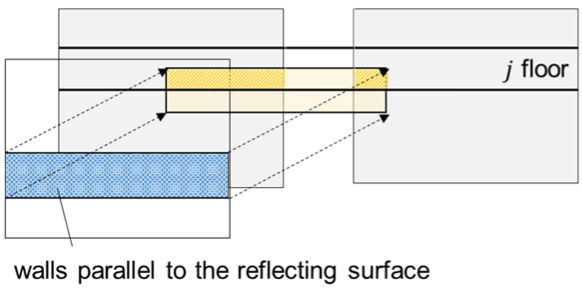

Computational Domain (top view)

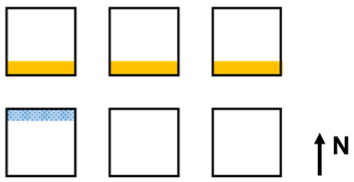

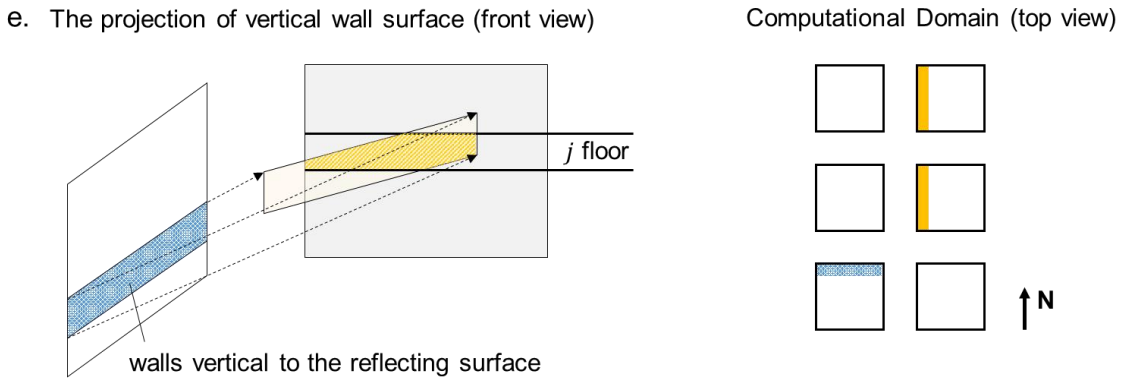

Figure 3.4. The projections and computational domains of each surface. (a) road between building wall; (b) crossing road; (c) roof; (d) parallel walls; (e) vertical walls

Figure 3.5 illustrates the projection of road surface onto the adjacent south-facing wall along the reflected solar beam at 8:00 and 11:00 in a summer day. At 8:00, the shape of *j*-floor projection shape consists of a hexagon and two triangles while it becomes a trapezoid at 11:00. The phenomenon that the shape and composition of projection varies with time makes it extremely complex to obtain time-varying value of projection area. One general method is to determine the projection shape and composition first, then calculate the area of each component respectively and finally add them up to obtain the total area of projection. However, this method is inefficient and the automatic recognition of projection shape and composition in the first step is difficult to implement by programming in Fortran.

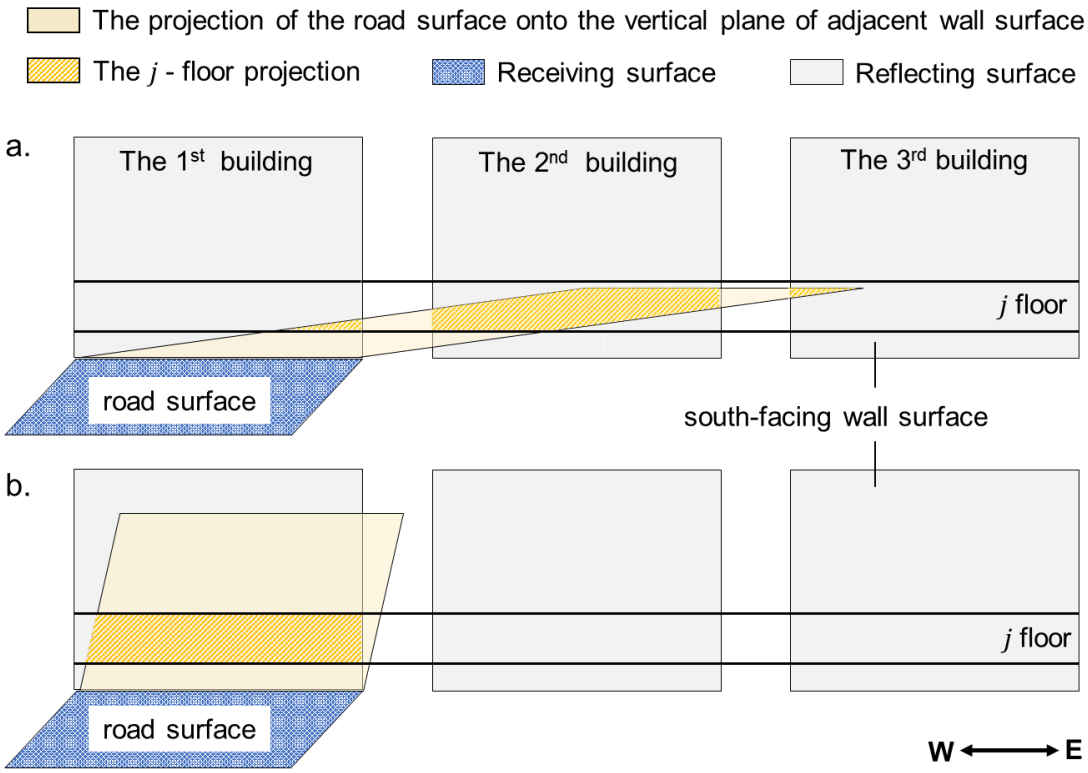

Figure 3.5. Time variation of the projection of a road surface onto the adjacent south-facing wall along the reflected solar beam at 8:00 and 11:00 in a summer day.

For this reason, a new method using analytic geometry was developed to simplify the computation process and compute the projection area more efficiently in a numerical way.

① A local coordinate system is established with the left side of the first building as y axis, the bottom side of the buildings as x axis and the intersection point of these two sides as origin. The left side of the projection intersects the upper side of jth floor, the top side of the projection and the lower side of jth floor at point O, M and Q respectively; The right side of the projection intersects these three sides at point P, N and R. The jth floor projection is divided into several small triangles and rectangles by 6 vertical lines $x = x_Q$, $x = x_M$, $x = x_b$, $x = x_c$, $x = x_R$, $x = x_N$. Since the position of each vertical line varies with time and value of j, x-coordinate of these lines is then arranged in an ascending sort order and indicated with x_i $(i = 1, n)$. Where n is determined by the numbers of buildings from which reflected solar beams can reach the receiving surface with high probability.

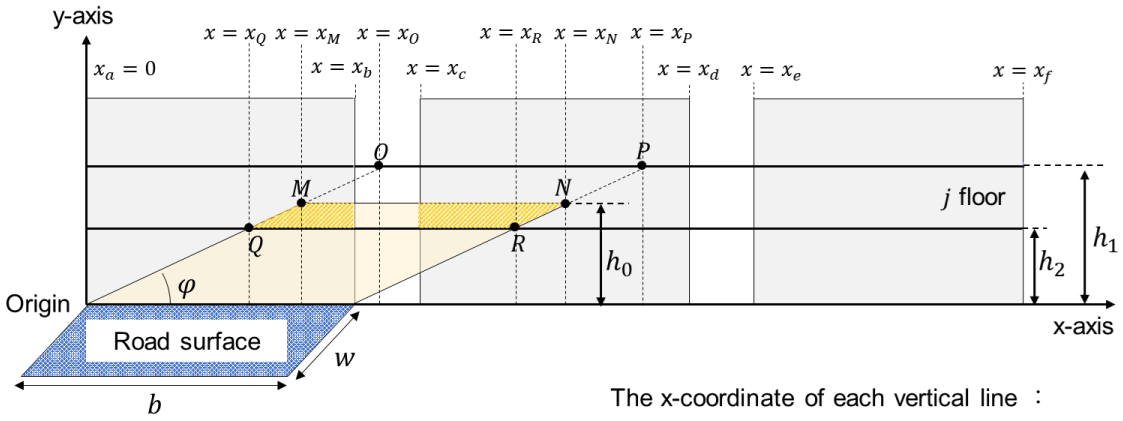

h_1 : Height of the upper side of the j floor
h_2 : Height of the lower side of the j floor
h_0 : Height of the projection
α : Solar azimuth angle
β : Solar elevation angle
φ : Angle of the projection to the ground

The x-coordinate of each vertical line :

$x_a = 0$
$x_b = b$
$x_c = b + w$
$x_d = 2b + w$
$x_e = 2b + 2w$
$x_f = 3b + 2w$

$x_O = h_1 / \tan\varphi$
$x_P = x_o + b$
$x_Q = h_2 / \tan\varphi$
$x_R = x_Q + b$
$x_M = h_0 / \tan\varphi$
$x_N = x_M + b$

② The line $x = x_i$ intersects the upper and lower sides of jth floor, the top, left and right sides of the projection at point A, B, C, D, and E respectively. The Δy_i , representing the length of left or right side of divided triangles and rectangles, is calculated using the following equation denotes

$$\Delta y_i = \min\{ y_{iA},\ y_{iC},\ y_{iD}\} - \max\{ y_{iB}, y_{iE} \}$$

Where y_{iA}, y_{iB}, y_{ic}, y_{iD}, y_{iE} denotes the y-coordinate of each point on the line $x = x_i$.

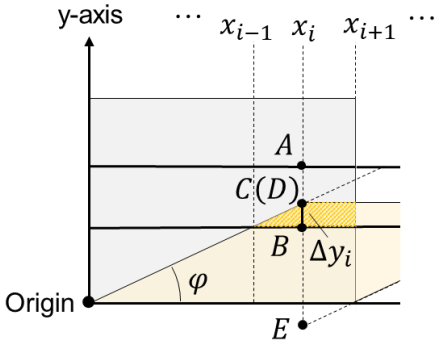

The y-coordinate of intersection point on the line $x = x_i$:

$y_{iA} = h_1$
$y_{iB} = h_2$
$y_{iC} = h_0$
$y_{iD} = x_i \tan\varphi$
$y_{iE} = (x_i - b) \tan\varphi$

$\Delta y_i = \min\{ y_{iA}, y_{iC}, y_{iD}\} - \max\{ y_{iB}, y_{iE} \}$

③ The area of divided triangles and rectangles between the line $x = x_i$ and $x = x_{i+1}$ are indicated with S_i and the total area of projection onto the jth floor wall are indicated with

S_j as shown in Fig. The value of S_i and S_j are calculated using the area formula as below

$$S_i = 0.5(\Delta y_i + \Delta y_{i+1})(x_{i+1} - x_i); \quad S_j = \sum_{i=1}^{n} S_i$$

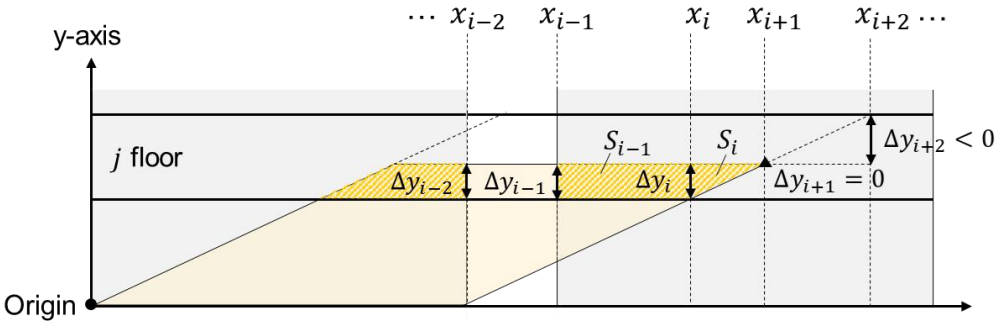

Area of each triangle and rectangle: $S_i = \frac{1}{2}(\Delta y_i + \Delta y_{i+1})(x_{i+1} - x_i)$

Total area of j -floor projection : $S_j = \sum_{i=1}^{n} S_i \quad (S_i > 0)$

④ Among all the beam solar reflection from jth floor wall, only that from the projection area can reach the receiving surface. If it is assumed that there is no energy loss of reflected solar beam during its propagation, then the proportion $P_d(j)$ can be determined by dividing the total area of jth floor projection by the receiving surface area.

$$P_d(j) = \frac{1}{A} S_j$$

Where A denotes the area of road surface receiving the solar reflection.

The projection areas of the roof and wall surfaces onto the adjacent wall are computed in the same way.

3.3.2 Specular reflection of diffuse component

Diffuse solar radiation is solar radiation reaching the Earth's surface after having been scattered from the direct solar beam by molecules or particulates in the atmosphere. Unlike the direct solar beams, the diffuse solar radiation has no directional dependence, as well as its specular reflection. That is to say, the proportion of specular reflection from the window surface to the receiving surface is a constant value and it only depends on the relative position

of these surfaces. To assess this value with shorter computational time, the calculation method of heat radiation transfer in a one-dimensional canopy model (Kondo and Liu, 2003) was utilized in this study. They assumed the windows surface as an ideal diffusely reflecting surface (Lambertian surface). In this way, the road, roof and wall view factors for the j-floor wall is equal to the proportion of reflected radiation received by these three surfaces. Hence, P_{s_j} of each receiving surface could be calculated from their view factors for the wall surface where the reflected beams come from. The details of the calculation of view factors can be seen in (Kondo and Liu, 2003)

However, it is need to be pointed out that the view factors obtained by Kondo and Akira' s method just represents the proportion of the diffusely reflected solar beams received by each surface. To obtain the value of the specular reflection, it needs to be adjusted by multiplying a correction coefficient. In this study, it is assumed that the diffuse solar radiation all comes from the upper hemisphere and are reflected down to the lower hemisphere through the specular reflection in a two-dimensional urban canopy. Under this assumption, for the same amount of reflected solar beams, the probability of the surfaces receiving the solar beams which is all reflected downward is twice that of diffusely reflected ones. Thus, the correction coefficient was set to 2.

3.4 Calculation of specular reflected solar radiation from window surface

In this study, it is assumed that all the retro reflection of solar radiation returns to the sky. In other words, they were not involved in the calculation of radiative heat transfer inside the urban canopy.

3.5 Calculation of angular-dependent reflectance, transmittance and absorptance

3.5.1 Method

As mentioned in section 4.2, the reflectance of direct solar beam $\rho_d(\theta)$ is angular dependent. its values are obtained with the function of solar incidence angle in this study. The experimental data (Harima and Nagayama, 2017b) was used to define the $\rho_d(\theta)$ function, using the quartic spline interpolation method. The function obtained is only the reflectance related to the direct component of the solar radiation and it is reported as below:

$$\rho_d(\theta) = a_4\theta^4 + a_3\theta^3 + a_2\theta^2 + a_1\theta + a_0$$

Where a_4, a_3, a_2, a_1, a_0 are coefficients determined by the experimental data of different types of window films and θ is the solar incidence angle to the window surface.

The reflectance of diffuse solar radiation is a constant value and it is obtained as indicated in the following equation (Siegel and Howell, 2001):

$$\rho_s = \frac{\int_{\theta=0}^{\theta=\pi/2} \rho_d(\theta)\cos\theta\sin\theta\, d\theta}{\int_{\theta=0}^{\theta=\pi/2} \cos\theta\sin\theta\, d\theta}$$

The transmittance is calculated by the same method as the reflectance. Since the sum of the reflectance (ρ), transmittance(τ) and absorptance(α) is equal to 1 for transparent surfaces, the absorptance is calculated by $1 - \rho - \tau$.

3.5.2 Empirical formulas of different window types

In this study, single-float glass without any films, single-float glass with heat shading films (HSF), and single-float glass with retro-reflective films (RRF) were used for evaluating the effect of different windows on the outdoor thermal environment and year-round energy consumption of air conditioning. The $\rho_d(\theta)$, $\tau_d(\theta)$ and $\alpha_d(\theta)$ function of each of them were

obtained using the measurement as shown in Table 3.1, Table 3.2 and Table 3.3. They were reported as follows:

Single-float glass:

$$\rho_{d\_f}(\theta) = 6.58841 \cdot 10^{-8}\theta^4 - 7.35996 \cdot 10^{-6}\theta^3 + 2.83089 \cdot 10^{-4}\theta^2 - 3.83618 \cdot 10^{-3}\theta + 8.64953 \cdot 10^{-2}$$

$$\tau_{d\_f}(\theta) = -6.14683 \cdot 10^{-8}\theta^4 + 6.89750 \cdot 10^{-6}\theta^3 - 2.66266 \cdot 10^{-4}\theta^2 + 3.45172 \cdot 10^{-3}\theta + 8.57859 \cdot 10^{-1}$$

Heat shading films (HSF):

$$\rho_{d\_h}(\theta) = 5.71590 \cdot 10^{-8}\theta^4 - 6.50793 \cdot 10^{-6}\theta^3 + 2.63516 \cdot 10^{-4}\theta^2 - 3.53511 \cdot 10^{-3}\theta + 1.69579 \cdot 10^{-1}$$

$$\tau_{d\_h}(\theta) = -2.26327 \cdot 10^{-8}\theta^4 + 1.75067 \cdot 10^{-6}\theta^3 - 5.21292 \cdot 10^{-5}\theta^2 + 3.25879 \cdot 10^{-4}\theta + 6.00593 \cdot 10^{-1}$$

Retro-reflective films (RRF):

$$\rho_{d\_r}^{total}(\theta) = 1.86049 \cdot 10^{-9}\theta^5 - 3.63864e-07\theta^4 + 2.59022 \cdot 10^{-5}\theta^3 - 6.88045 \cdot 10^{-4}\theta^2 + 4.79470 \cdot 10^{-3}\theta + 1.46911 \cdot 10^{-1}$$

$$\rho_{d\_r}^{down}(\theta) = 8.43039 \cdot 10^{-8}\theta^4 - 1.04600 \cdot 10^{-5}\theta^3 + 4.37347 \cdot 10^{-4}\theta^2 - 6.05674 \cdot 10^{-3}\theta + 7.76475 \cdot 10^{-2}$$

$$\tau_{d\_r}(\theta) = -2.33129 \cdot 10^{-8}\theta^4 + 2.02888 \cdot 10^{-6}\theta^3 - 5.07223 \cdot 10^{-5}\theta^2 + 3.38466 \cdot 10^{-4}\theta + 4.22009 \cdot 10^{-1}$$

$$\rho_{d\_r}^{up}(\theta) = \rho_{d\_r}^{total}(\theta) - \rho_{d\_r}^{down}(\theta)$$

$$\alpha_d(\theta) = 1 - \rho_d(\theta) - \tau_d(\theta)$$

Where, the subscripts f, h, and r denote to the single-float glass windows, heat-shading window and retro-reflective window respectively. Moreover, the function of retro reflectance obtained with the quartic spline interpolation method could not described its variation

precisely since it was not monotonous with the incident Angle. Hence, in order to improve the prediction accuracy, the value of retro reflectance $\rho_{d\_r}^{up}(\theta)$ was calculated by subtracting the specular reflectance $\rho_d(\theta)$ from hemispherical reflectance $\rho_d(\theta)$.

Table 3.1. Measurement data of the optical properties of retro-reflective films (RRF)

Incidence angle	Specular reflectance	Retro reflectance	Transmittance	Absorptance
0	0.091	0.065	0.422	0.422
5	0.080	0.063	0.422	0.435
10	0.076	0.063	0.422	0.439
15	0.075	0.064	0.422	0.439
20	0.071	0.064	0.421	0.445
25	0.067	0.064	0.421	0.447
30	0.064	0.065	0.423	0.448
35	0.052	0.066	0.425	0.457
40	0.055	0.071	0.425	0.448
45	0.094	0.083	0.423	0.400
50	0.135	0.096	0.418	0.351
55	0.150	0.110	0.408	0.332
60	0.153	0.133	0.393	0.321
65	0.153	0.171	0.373	0.303
70	0.143	0.235	0.340	0.281
75	0.128	0.333	0.288	0.251
80	0.110	0.476	0.206	0.208
85	0.072	0.681	0.097	0.149
90	0	1	0	0

Table 3.2. Measurement data of the optical properties of heat shading films (HSF)

Incidence angle	Specular reflectance	Retro reflectance	Transmittance	Absorptance
0	0.161	/	0.161	0.600
5	0.163	/	0.163	0.602
10	0.162	/	0.162	0.601
15	0.161	/	0.161	0.599
20	0.161	/	0.161	0.597
25	0.162	/	0.162	0.594
30	0.165	/	0.165	0.592

35	0.170	/	0.170	0.589
40	0.176	/	0.176	0.584
45	0.185	/	0.185	0.576
50	0.199	/	0.199	0.564
55	0.218	/	0.218	0.546
60	0.247	/	0.247	0.518
65	0.291	/	0.291	0.479
70	0.354	/	0.354	0.425
75	0.445	/	0.445	0.354
80	0.575	/	0.575	0.262
85	0.755	/	0.755	0.145
90	1	/	1	0

Table 3.3. Measurement data of the optical properties of single float glass (SFG)

Incidence angle	Specular reflectance	Retro reflectance	Transmittance	Absorptance
0	0.078	0.006	0.072	0.865
5	0.079	0.006	0.073	0.864
10	0.078	0.006	0.072	0.865
15	0.076	0.005	0.071	0.866
20	0.074	0.004	0.070	0.866
25	0.074	0.004	0.070	0.865
30	0.074	0.003	0.071	0.864
35	0.076	0.002	0.074	0.861
40	0.080	0.002	0.078	0.857
45	0.087	0.002	0.085	0.850
50	0.098	0.001	0.096	0.840
55	0.116	0.002	0.115	0.822
60	0.146	0.002	0.144	0.794
65	0.193	0.002	0.191	0.750
70	0.263	0.002	0.261	0.685
75	0.366	0.002	0.364	0.588
80	0.513	0.002	0.511	0.451
85	0.719	0.001	0.718	0.260
90	1	0	1	0

3.5.3 Results

Figure 3.6 shows the variations of reflectance, transmittance and absorptance with incidence angles on the different window surfaces. It is obtained by the empirical formulas mentioned Above. For all windows, the specular reflectance increases with the increase of incidence angle to the window surface while the transmittance and absorptance decreases with the increase of incidence angle. The retro reflectance increases first as the incident angle increases and maximizes at an angle of 60°. Afterwards, it drops gradually and turns into 0 at an angle of 90°.

The average value of specular reflectance, retro reflectance, transmittance and absorptance of each type of window were listed in Table 3.4. The Single-float glass proposed the highest transmittance (0.682) and the lowest absorptance (0.050) and specular reflectance (0.268) among them. Compared with the HSF, the RRF had the higher transmittance and lower absorptance as well as specular reflectance. However, the hemispherical reflectance of RRF (0.354) and HSF (0.350) was almost no difference.

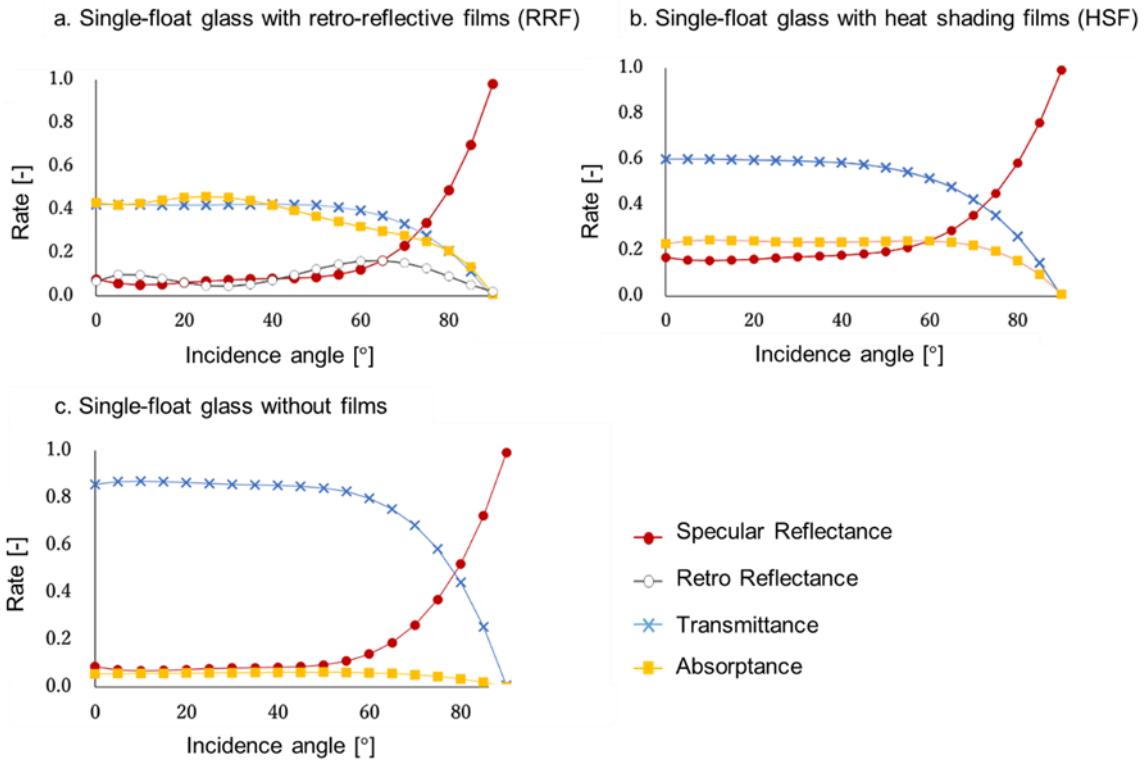

Figure 3.6 Variations of reflectance, transmittance and absorptance with incidence angles to window surface. (a) Single float glass with retro-reflective films (RRF); (b) Single float glass with heat shading films (HSF); (c) Single float glass

Table 3.4. The average values of the optical properties of each window surface

	Specular reflectance	Retro reflectance	Transmittance	Absorptance
Single-float glass	0.268	/	0.682	0.050
Single-float glass with HSF	0.350	/	0.446	0.204
Single-float glass with RRF	0.251	0.103	0.333	0.313

CHAPTER 4. VALIDATIONS OF PROPOSED MODEL

4.1 Validation method

In the previous section, the method of radiation heat transfer analysis considering the specular and retro reflection was described. The validation of the proposed calculation method should be conducted before further application.

The data obtained by CM model in this study is the average value of the whole block, which require the measurement data being acquired on the condition of the urban-block-scale introduction of RRF. However, RRF, as a new type of transparent window film that can reflect shortwave solar rays upwards, has not been widely used. Thus, the simulated results using CFD model (Yoshida and Moshida, 2017; Yoshida et al, 2018) were used to compare with the results in this study for the validation of proposed method.

Yoshida and Mochida evaluated retro-reflective film on thermal environment in outdoor spaces by CFD analysis coupled with radiant computation. In their study, the directional reflection of solar radiation was computed using AND model (Makino et al, 1999) with a great quantity meshed of ground and building surfaces. Thus, the simulated results in their study has a high accuracy and reliability.

The comparison was conducted by the following items:

- The diurnal variation of retro reflectance of the west-facing window
- The impact of the consideration of specular reflection on
    - Reflected solar radiation incident on the pedestrian' body surface
    - Air temperature, road surface temperature and wall surface temperature
    - MRT

The simulation conditions were set to be the same as those in Yoshida's research, including the geometry parameters of block, meteorological data and window types.

4.2 Simulation conditions

4.2.1 Urban block model

Figure 4.1 illustrates the front view and top view of a three-dimensional city block model in this analysis. The 30-m-wide and 30-m-high buildings stand on a lattice array in a 500m x 500m square computational domain. The distance between buildings was 30m. The window that has a property for directional reflection of solar radiation was installed to the western exterior wall of each building and the window to wall ratio was set to 80%. In order to eliminate interference with the directional reflection on the window surfaces, the other window shades such as curtains and blinds were not considered in this study. In addition, the other wall surfaces were made of concrete materials with a diffuse reflectance of 0.2 and the road was covered with asphalt and concrete with an average reflectance of 0.12.

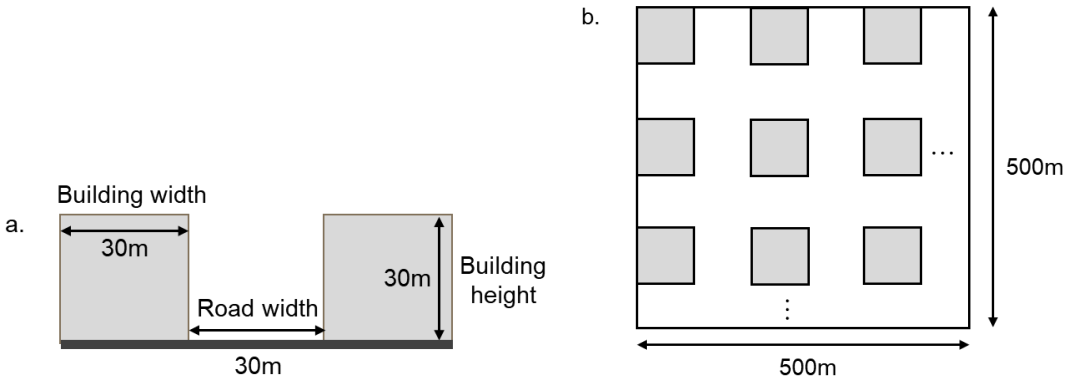

Figure 4.1. The city block model in the analysis for the verification of the proposed calculation method (a). Front view (b). Top view

4.2.2 Meteorological data

The analysis started from July 27 to August 31, 2006 using the meteorological data obtained from WRF model. As Yoshida investigated the thermal environment on a particularly hot summer day (July 23, 2010) in Tokyo, the day with the most similar weather conditions (August 5, 2006) was chosen as target date. Table 4.1 shows the comparison of meteorological data for July 23, 2010 and August 5, 2006 (Japan Meteorological Agency). Both two days are nearly cloudless sunny days.

Table 4.1. Weather data for July 23, 2010 and August 5, 2006 (Japan Meteorological Agency)

	Average temp. (° C)	Maximum temp. (° C)	Minimum temp. (° C)	Total precipitation (mm)
July 23, 2010	30.8	35.7	26.8	0
August 5, 2006	30	35.4	25.3	--

	Total solar radiation (MJ/m^2)	Average humidity (%)	Average cloudiness (10 minutes ratio)	Weather condition (6:00~18:00)
July 23, 2010	23.9	65	2	sunny
August 5, 2006	24.1	57	0	sunny

4.2.3 Simulation cases

In this analysis, the following three cases were investigated. As shown in Table 4.2, in Case1 and Case2, it was assumed that single-float window without any window films was used. In Case3, single-float window with a retro-reflective film (RRF) was used. Besides, in Case1, the windows surface was considered as perfectly diffuse surfaces with a constant reflectance while the directional reflection characteristics of window surface was considered in Case2 and Case3.

Table 4.2. Simulation cases for the validations of proposed model

	Case1	Case2	Case3
Window type	Single float glass	Single float glass	RRF
Refection type	Diffuse reflection	Directional reflection	

4.3 Diurnal variation of retro reflectance of the window with different orientations

Figure 4.2 shows the diurnal variations of the specular, retro and hemispherical reflectance of the retro-reflective window with different orientation on a typical summer day. The window surfaces of four main orientation N, S, W and E were irradiated in the different time period: 5:00 -12:00 (E), 12:00-19:00 (W), 8:00-16:00 (S), 5:00-8:00 and 16:00-19:00 (N). Hence, the values for reflectance were obtained during the corresponding period. The retro reflectance reached the maximum at approximately 10:00 for east-facing window and approximately 14:00 for west-facing window, with nearly the same value of 0.159 and 0.158 respectively. For south-facing window, the retro reflectance peaked at approximately 8:00 and 16:00, and reduced to a relatively low value around noon. For north-facing window, the maximum value of retro reflectance happened at the same time as south-facing window.

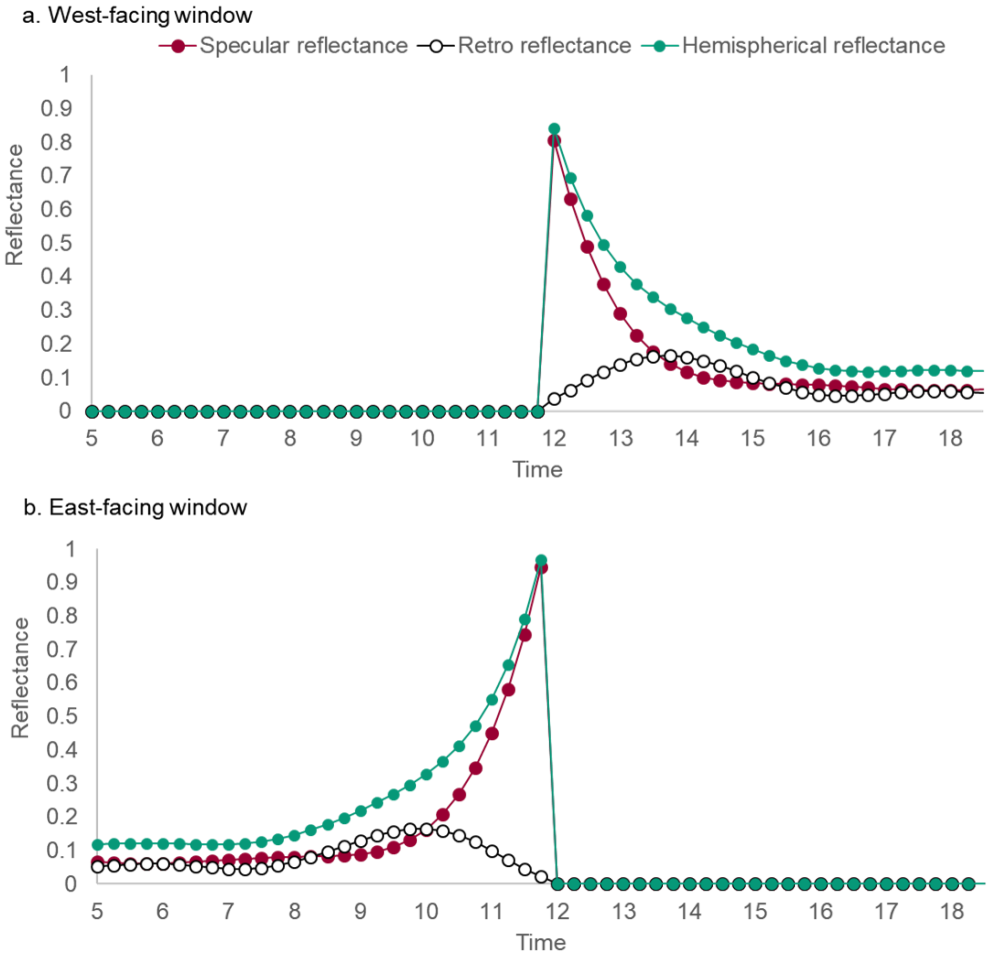

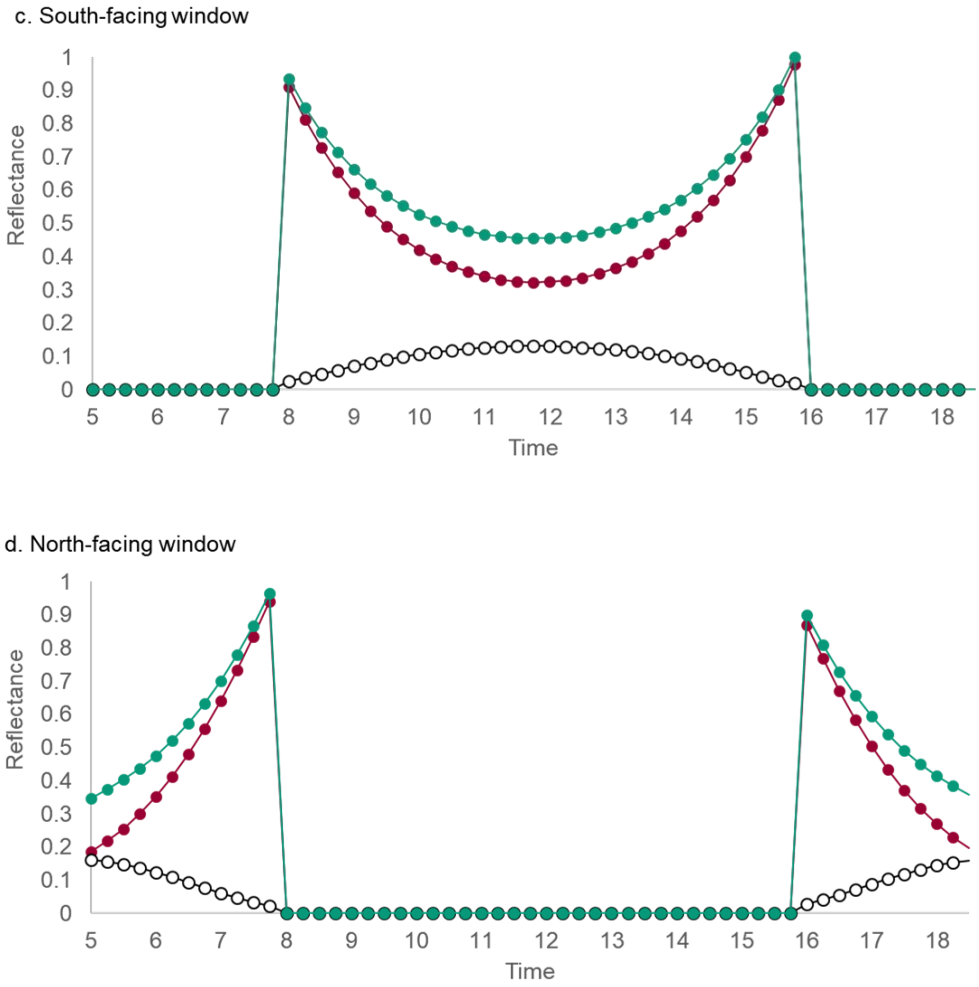

Figure 4.2. Diurnal variations of the specular, retro and hemispherical reflectance of the retro-reflective window facing different directions on August 5,2006. (a) West-facing window; (b) East-facing window; (c) South-facing window; (d) North-facing window

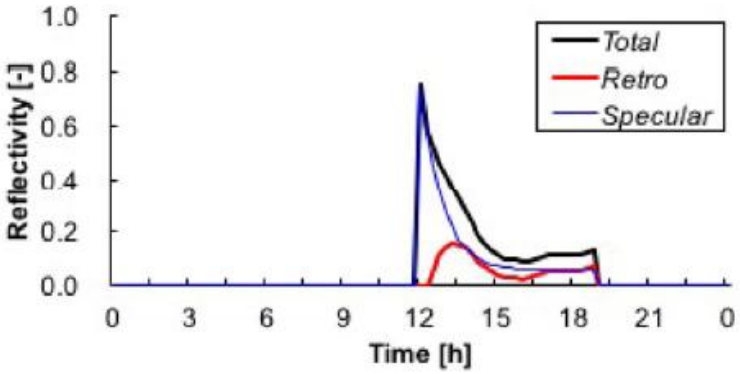

Figure 4.3. Time variations of total, retro, and specular reflectivity of the retro-reflective window facing the western direction on July 23, 2010 (Yoshida et al, 2018)

In the Yoshida's study, the results of reflectance variation of retro-reflective west-facing window was shown in Figure 4.3. The retro reflectance reaches the maximum value of 0.16 at approximately 14:00, which is same as the results obtained in my study.

4.4 Impact of the specular reflection of solar radiation on outdoor thermal environment

4.4.1 Reflected solar radiation incident on the pedestrian' body surface

There are two forms of the radiation incident on the pedestrian's body surface. The first one is shortwave radiation, including the direct solar radiation, diffuse solar radiation, and reflected solar radiation from the surfaces that surround the pedestrian in the built environment. The second one is longwave radiation, including longwave atmospheric counter radiation and longwave emission from building and ground surfaces. The consideration of the specular reflection of solar radiation increase the downward reflected shortwave reflection, which result in the change of the radiation absorbed by the ground and wall surface and their surface temperature. For this reason, the values of direct solar radiation, diffuse solar radiation and longwave atmospheric counter radiation calculated by the new model are the same as those calculated by the model considering the window surface as perfectly diffuse surfaces, as well as the reflected solar radiation from ground surface since it is covered with asphalt and concrete, which don not have the property for directional reflection of solar radiation. Thus, in the Figure 4.4, Only the reflected shortwave radiation from wall surfaces, longwave radiation from ground surfaces and from wall surfaces were investigated.

Figure 4.4 illustrates the change of radiation per unit area received by pedestrians in the outdoor space after considering the specular reflection of solar radiation from window surfaces on August 5, 2006. The amount of radiation change is also calculated by subtracting the amount of radiation in Case 1 (single-float window treated as perfectly diffuse surfaces) from that in Case2(single-float window considering the property of specular reflection). Due to the consideration of downward specular reflection of solar radiation, the shortwave radiation reflected from wall surface and longwave radiation emitted by ground surface increased obviously at approximately 14, while the longwave radiation from wall surface decreased slightly at the same time. The radiation variations were caused by the increase in the ground surface temperature and reduction in the wall surface temperature as showed in Figure 4.5

Table 4.3 shows the amount of the radiation incident on the pedestrian's body surface in Case1 and Case2 at 14:00. In the total amount of incident radiation change (+16.5 W/m^2), shortwave solar reflection from the wall surfaces (+13.4 W/m^2) accounted for approximately 80% and the longwave emission from road and wall surfaces (+3.0 W/m^2) accounted for 20%. Moreover, compared to the result in Case1, the shortwave radiation reflected from the wall surfaces increased approximately 1.5 times while the long wave radiation emitted from

the wall and the road surfaces did not change much.

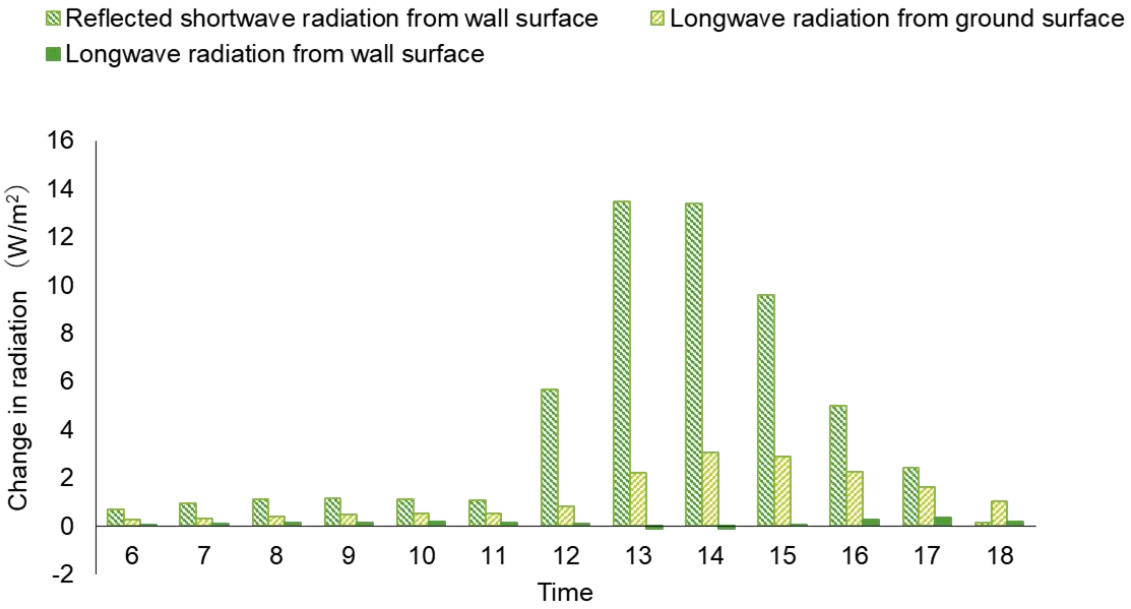

Figure 4.4. Changes of the Reflected solar radiation incident on the pedestrian' body surface due to the consideration of specular reflection of solar radiation on August 5, 2006

Table 4.3. Amount of the radiation incident on the pedestrian body surface in Case1 and Case2 at 14:00 (Units: W/m^2)

	Case1	Case2	Δ
Reflected shortwave radiation from wall surface	8.9	22.3	+13.4
Longwave radiation from ground surface	615.4	618.5	+3.1
Longwave radiation from wall surface	214.9	214.8	−0.1

For the reflected solar radiation incident on the pedestrian body surface, the results in (Yoshida and Moshida, 2017) was 15.5 W/m^2 (13.4 W/m^2 in my study).

4.4.2 Air temperature, road surface temperature and wall surface temperature

Figure 4.5 illustrates the change of the road surface temperature, wall surface temperature and air temperature at 3m above the ground after considering the specular reflection of solar radiation from window surfaces on August 5, 2006. The surface temperature and air temperature in Case1 and Case2 are average value of the whole block. The temperature

difference between these two cases is calculated by subtracting the value in Case 1 (single-float window treated as perfectly diffuse surfaces) from that in Case2 (single-float window considering the property of specular reflection).

Due to the consideration of downward specular reflection of solar radiation, the average road surface temperature increased rapidly from noon and reached a maximum of 0.4 ℃ at 14:00 (The value of temperature change was positive) while the average wall surface temperature decreased around 14 (The value of temperature change was negative). It is because at approximately 14:00 in a summer day, the sun altitude angle is very high, the specular reflection of solar radiation from window surfaces concentrates on the road surface. As a result, the amount of solar reflection incident on the adjacent wall surface is less than that when the solar radiation reflected diffusely off the window surfaces, which make the average wall surface temperature reduce. The difference of average air temperature at 3m above the ground between Case1 and Case2 was not obvious.

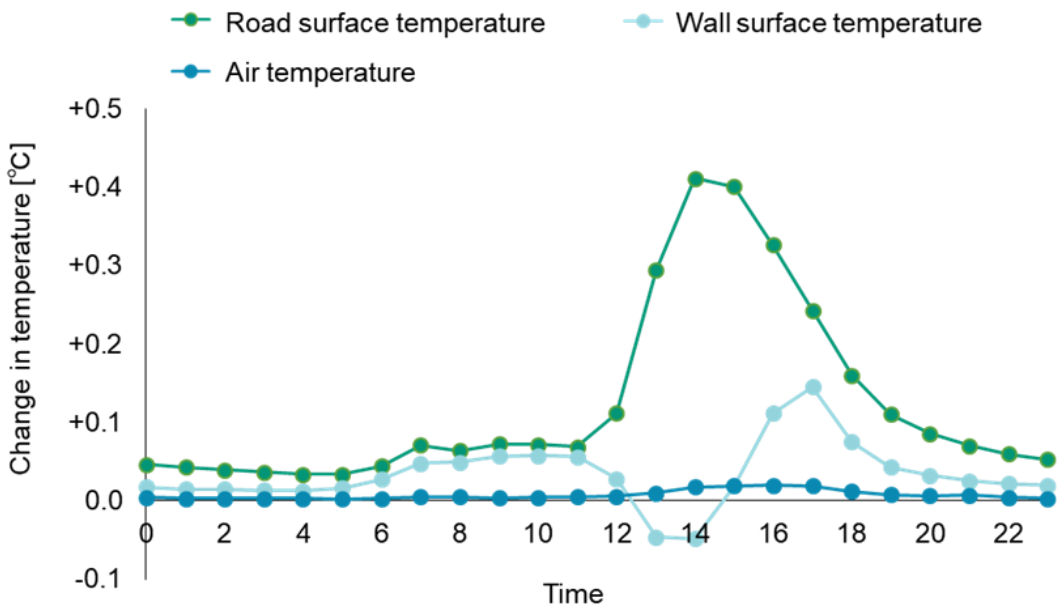

Figure 4.5. Time variations of the air temperature at 3m above the ground and average surface temperature of road and building walls after considering the specular reflection of solar radiation from window surfaces on August 5, 2006.

The same results could be observed in (Yoshida and Moshida, 2017) and (Nakaohkubo et al, 2008)

4.4.3 MRT

Figure 4.6 illustrates the time variation of MRT drop (3m above the ground) due to the consideration of the specular reflection of solar radiation from window surfaces on August 5, 2006. The MRT drop increased rapidly from noon and reached a maximum of 0.7 ℃ at 14:00. In the analysis, the window was installed to the western exterior wall of the building which is irradiated only in the afternoon. Hence, a large amount of direct solar radiation incident on west-facing window begin to be reflected downward after that, which results in the variation as showed in the figure.

The value of MRT drop at 14:00 obtained by Yoshida (Yoshida and Moshida, 2017) was 0.8 ℃ (0.7 ℃ in my study)

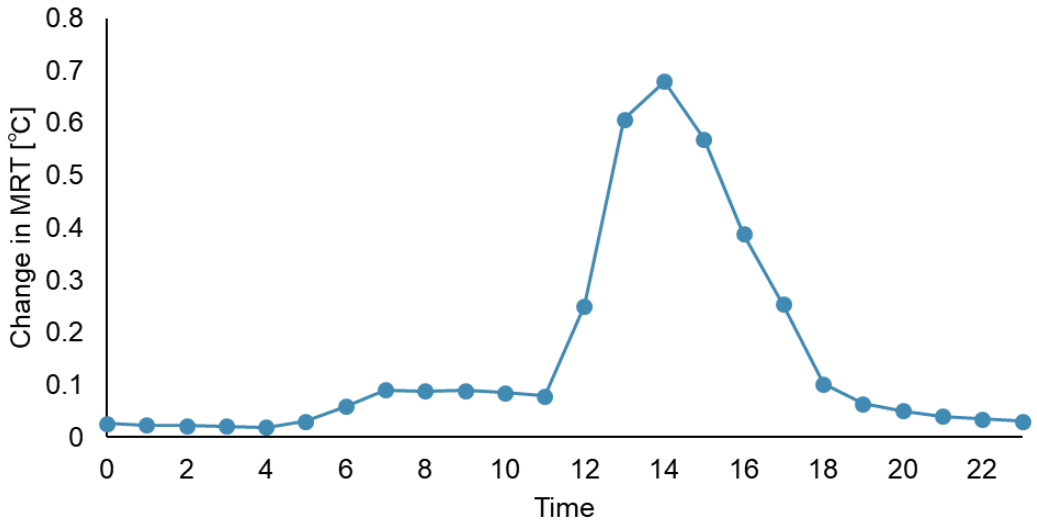

Figure 4.6. Time variations of MRT (3m above the ground) due to the consideration of specular reflection of solar radiation from window surfaces on August 5, 2006.

4.5 Conclusions

By comparison, it is indicated that the diurnal variation of retro reflectance of the west-facing window was reproduced precisely using proposed model. For the impact of the consideration of specular reflection on the outdoor thermal environment, the results calculated by proposed model are a little smaller than that obtained with CFD model (Yoshida and Moshida, 2017). The difference between them is due to the limitation of the proposed model that not all adjacent building walls are involved in the compactional domain as shown in Figure 3.4.

Considering the fact that weather data is not exactly the same between July 23, 2010 and August 5, 2006, the above result is reliable to some extent and the validity of the proposed model was verified

CHAPTER 5. EFFECTS ON THE OUTDOOR THERMAL ENVIRONMENT IN THE 23 WARDS OF TOKYO

5.1 Description of simulation cases

In this analysis, the Tokyo GIS data (Tokyo, 2013) needs to be converted into the form that can be inputted into the CM-BEM model. The urban blocks were classified into three types: office and commercial buildings block, apartment block and detached house block, according to land uses and the main purpose of buildings in each urban block. The size of each block was 500m × 500m. Figure 5.1 shows the distribution of urban blocks with three building types as 0.5-km grids in the 23 wards of Tokyo. Overall, the office and commercial building blocks concentrated in the center of the city, surrounded by the apartment blocks. And most of detached house blocks were farthest from the central part among these three block types. The blank grids on the figure were the blocks not being simulated, in which the most lands are occupied by parks and forests, or mainly used for industrial premises.

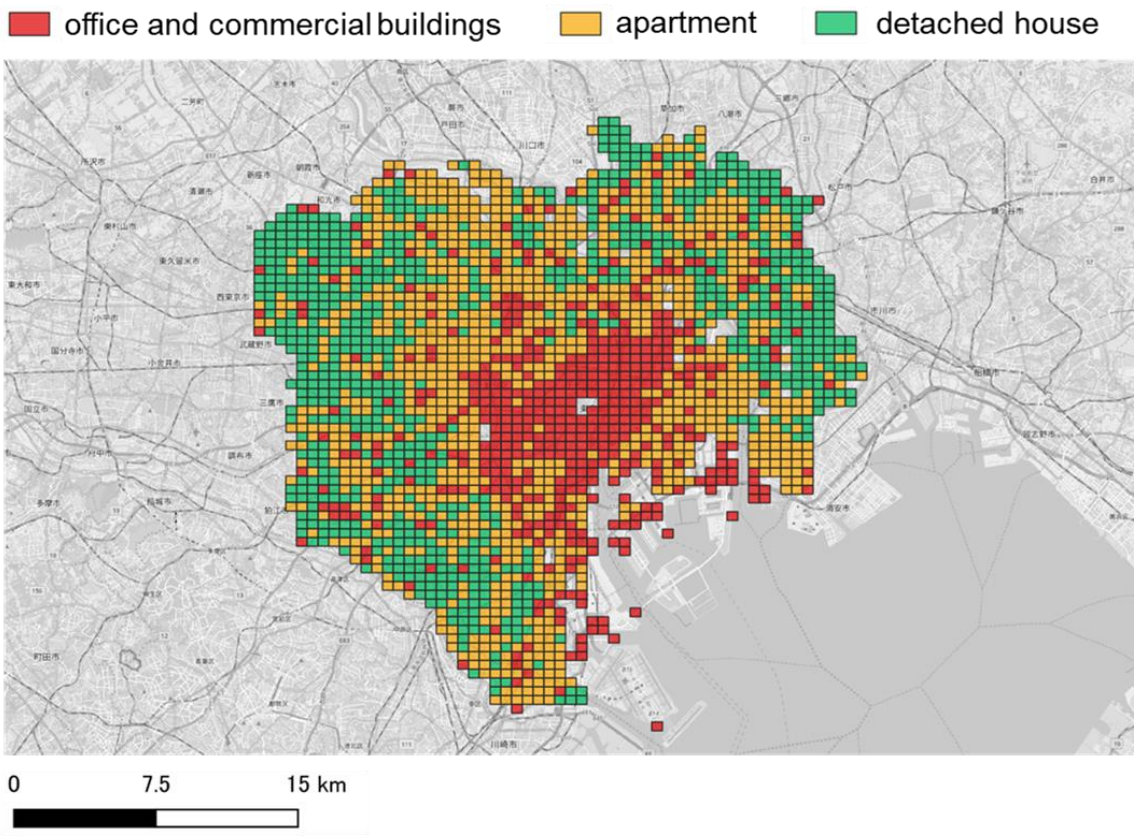

Figure 5.1. Distributions of building types as 0.5-km grids in the 23 wards of Tokyo

Since the retro-reflective window films are more commonly applied to the buildings with high window to wall ratios, the effects of RRF on outdoor thermal environment were evaluated only in the office and commercial building block (Figure 5.2) with the window to wall ratio of 0.33. The total number of simulated blocks was 465. Considering the increase of newly built buildings constructed by glass curtain wall in the center business district, the scenario with the window to wall ratio of 0.9 was also simulated in this section.

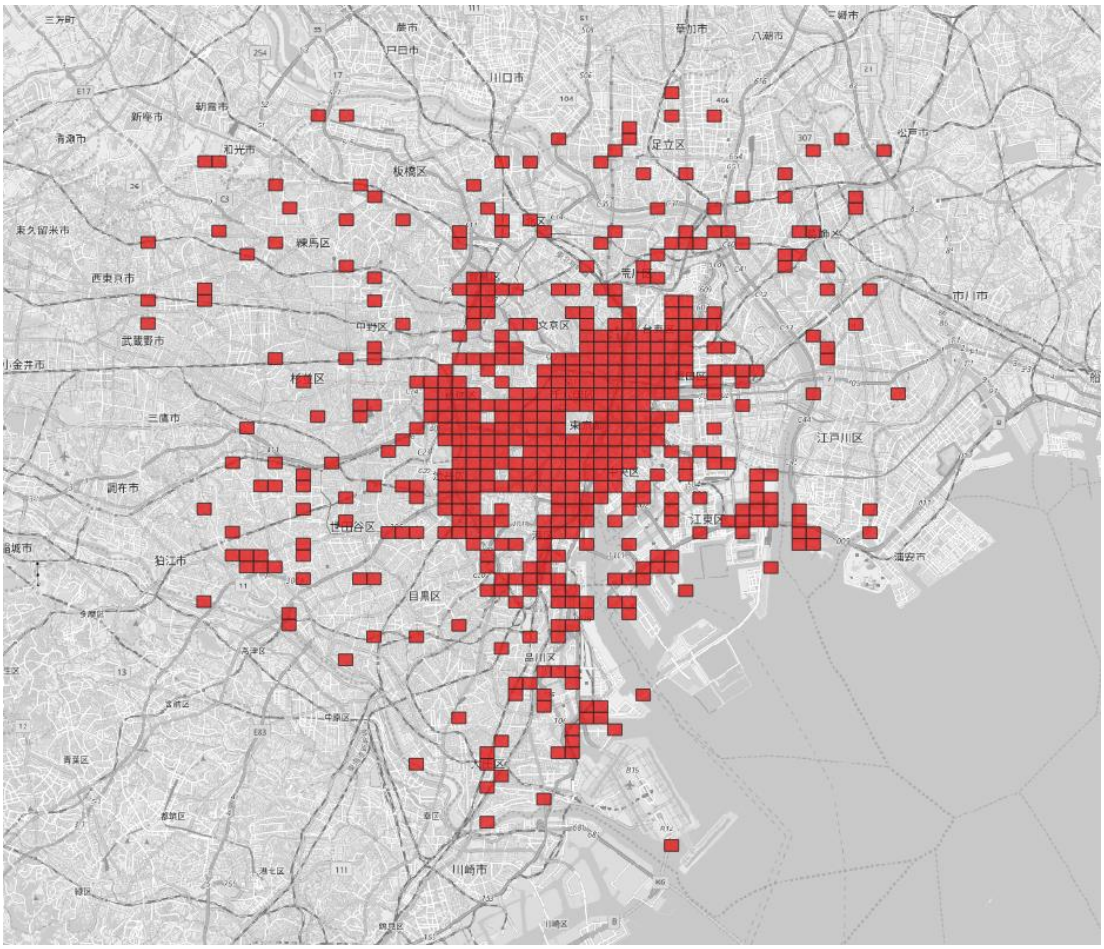

Figure 5.2. Distributions of office and commercial building blocks as 0.5-km grids

In the previous studies, it is indicated that comparing the single float glass window without any films, the thermal environment in outdoor space deteriorates as a result of the installation of retro-reflective films (Yoshida et al, 2018). Hence, the effect of RRF on thermal environment was compared with HSF in this analysis. Two cases were investigated: Case1 (HSF), Case2 (RRF). And in both cases, the window was installed to the building walls with four orientation E, W, S and N.

5.2 Time variation of effects on the thermal environment

Figure 5.3 Time variation of MRT (HSF) and Δ MRT (HSF-RRF) on August 5, 2006 and Figure 5.4 shows the results of WBGT. Both were the average value of the office and commercial building blocks in Tokyo 23 wards. The value of Δ MRT (HSF-RRF) increased significantly at 9:00 (0.29 ℃) and 15:00 (0.26 ℃), while it became not obvious at approximately noon when the radiant environment was worst with the highest value of MRT. The difference was caused by the reduction in the proportion of solar radiation reflected upwards around noon, at which the solar radiation gains of the windows with east and west orientation decreased and their retro reflectance also became lower as showed in Figure 4.2. The value of average MRT reached nearly 64.3℃ at 12:00, indicating the most severe radiant environment in a day. For WBGT, the value of Δ MRT (HSF-RRF) increased during the time period of 14:00 and 16:00 when the outdoor thermal comfort was still at a low level with a high value of WBGT.

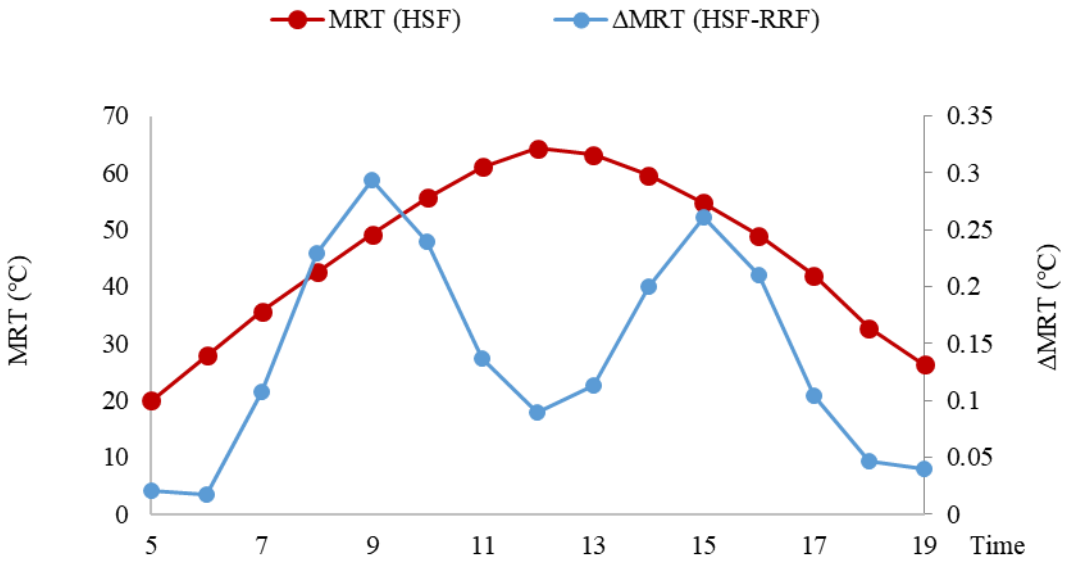

Figure 5.3. Time variation of MRT and Δ MRT (HSF−RRF) on August 5, 2006

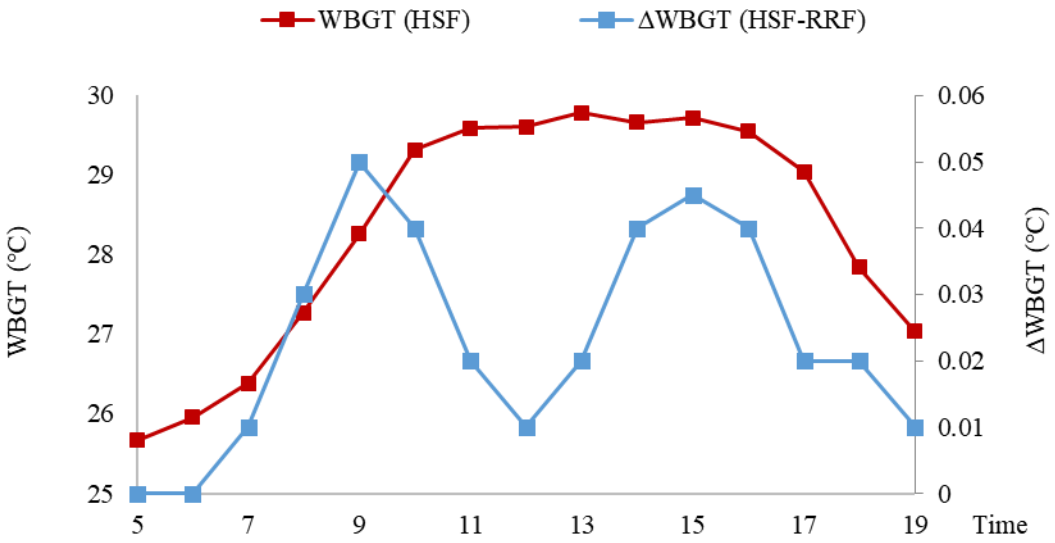

Figure 5.4. Time variation of WBGT and Δ WBGT (HSF−RRF) on August 5, 2006

5.3 Geographical distribution of effects on the thermal environment

In this part, the result of improvement effect on thermal environment in each office and commercial building block was presented on a grids map. Figure 5.5 shows the distribution of MRT drop at 15:00 as a result of the installation of RRF. The average value of MRT drop of all office and commercial building blocks was 0.25 ℃. And the maximum MRT drop happened in the block located in commercial areas near the Okachimachi Station, with the value of 0.45 ℃. In the figure, the blocks where the MRT drop a lot concentrated in the Taido and Chuo wards. The following map as showed in Figure 5.6 was made by Tokyo Environment Bureau in 2005 (Tokyo Environment Bureau, 2005). They analyzed the influence of anthropogenic heat and ground cover on the outdoor thermal environment. The red, orange and yellow grids represent the office and commercial areas. The closer the color is to red, the worse the thermal environment it is. By comparing this figure with the results obtained in my study, it can be found that it showed a high degree of overlap between the areas where the MRT drop a lot and areas with severe thermal environment.

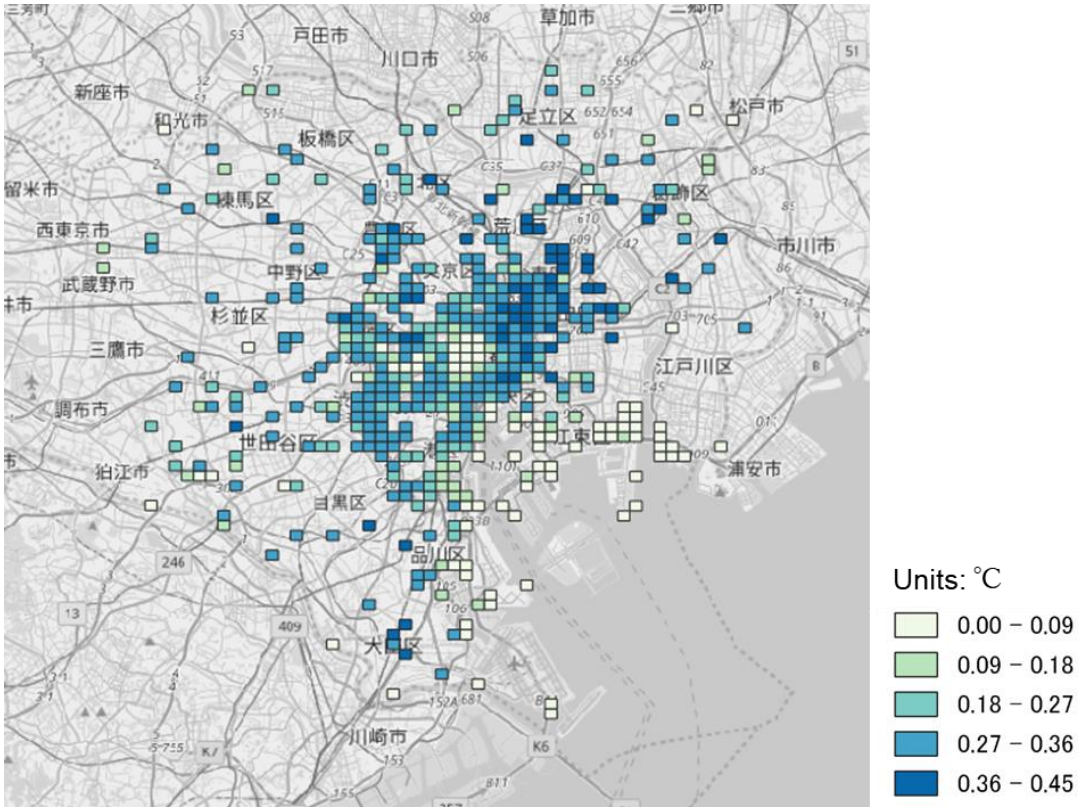

Figure 5.5. Distribution of MRT drop at 15:00 as a result of the installation of RRF on August 5 (only office and commercial building blocks was showed)

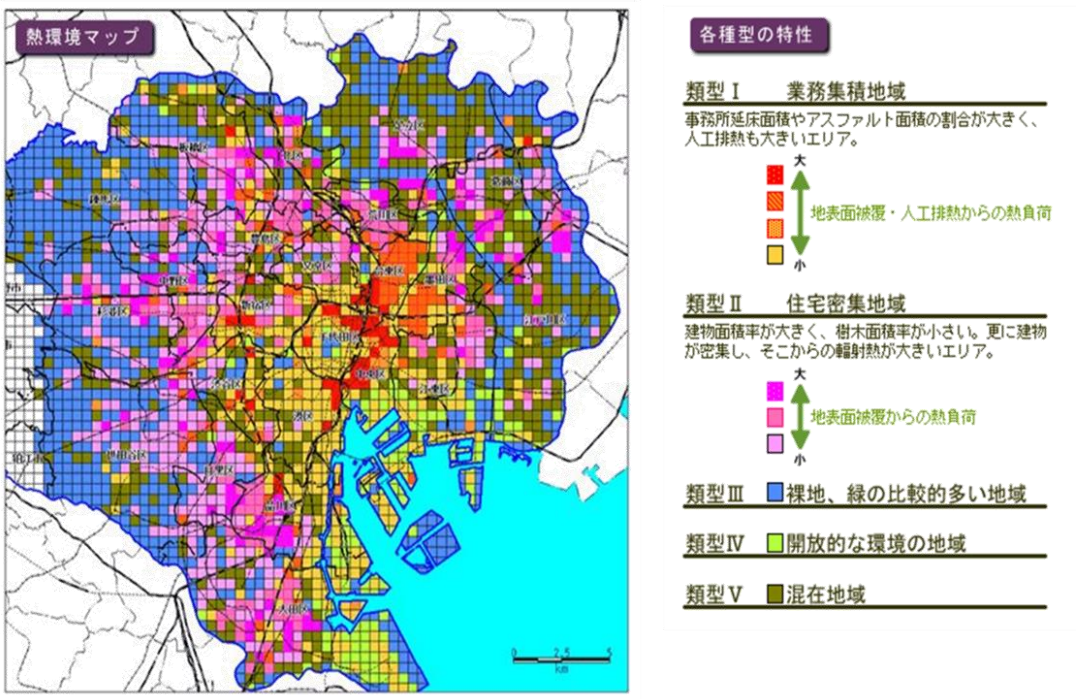

Figure 5.6. Thermal environment map of Tokyo 23 wards (Tokyo Environment Bureau, 2005)

5.4 Impact of urban geometry on the improvement effect

Due to the principle of improvement effect of RRF on the outdoor thermal environment, it can be inferred that there is a strong relationship between the urban geometry and that improvement effect. In this part, correlation analysis was conducted first, using the building coverage, aspect ratio and average building height, as morphological parameters. Then, a simple prediction models of the MRT drop as a result of the installation of RRF was established by regression analysis method.

5.4.1 Distributions of urban geometry parameters

Building coverage defined as the ratio of building area to the total land area, is usually used to describe the urban horizontal density. The building coverage of office and commercial building blocks in Tokyo 23 wards was in a range from 0.1 to 0.5 with the average value of approximately 0.3. Another key parameter in determining urban geometry is aspect ratio, which is defined as the ratio between the average building height (H) and the road width (W). The urban canopy is considered uniform if it has an aspect ratio of approximately 1, deep of the aspect ratio is equal to 2, and shallow if the canyon has an aspect ratio below 0.5 (Lai et al., 2019) The average aspect ratio of office and commercial building blocks was in a range from 0.15 to 3.6 with the average value of approximately 1.5. Additionally, the average height (H) of office and commercial building blocks was in a wide range from 7m to 51m with the average value of approximately 13.

The distributions of shape indices of office and commercial building blocks were showed in Figure 5.7 The grid color became darker as the index value increase. In the figure, the block processing high-rise building clusters near Shinjuku station could be distinctly identified. And the crowded commercial blocks in Asakusa-Ueno areas could also be located easily on the map. Figure 5.5 shows the distribution of MRT drop at 15:00 as a result of the installation of RRF. Comparing these two figures, it can be found that most of the blocks where the MRT dropped a lot concentrated on the high vertical density areas with large values of building coverage. While the relationship between MRT drop and other two shape parameters was not so obvious.

Hence, in the following part, building coverage, aspect ratio and average building height were tested for the correlation with the MRT drop at 15:00 by means of regression analysis, respectively.

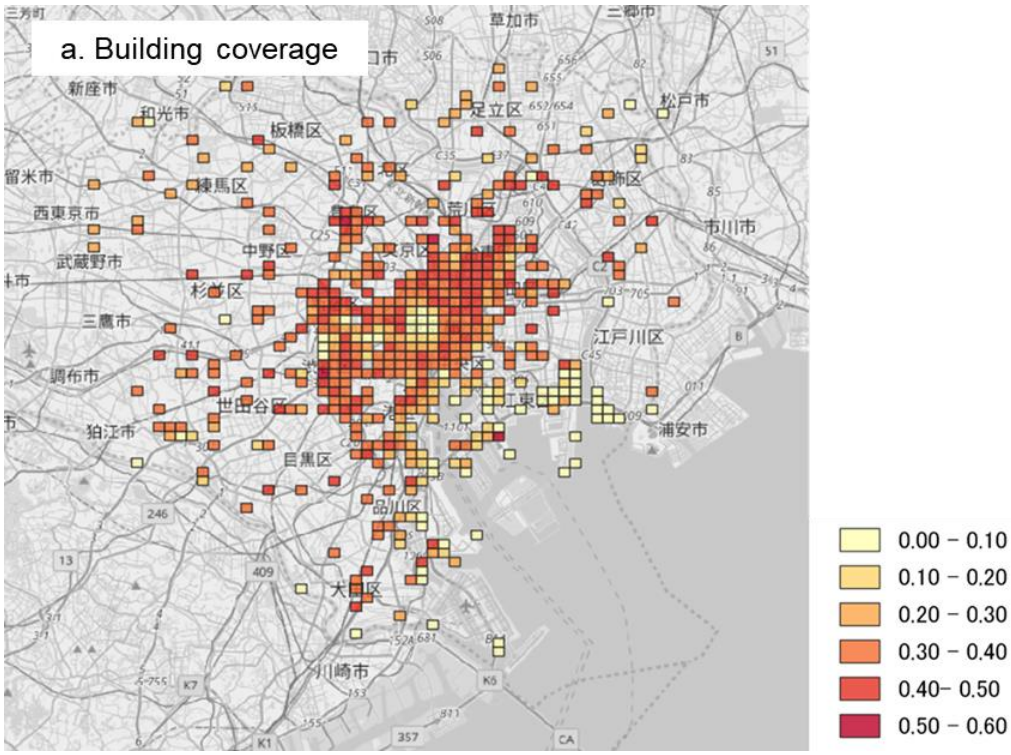
a. Building coverage
草加市
三郷市
新座市
和光市
板橋区
足立区
松戸市
練馬区
西東京市
市川市
武蔵野市
中野区
杉並区
三鷹市
江戸川区
調布市
世田谷区
浦安市
狛江市
巨黒区
品川区
大田区
川崎市
0.00 – 0.10
0.10 – 0.20
0.20 – 0.30
0.30 – 0.40
0.40– 0.50
0.50 – 0.60

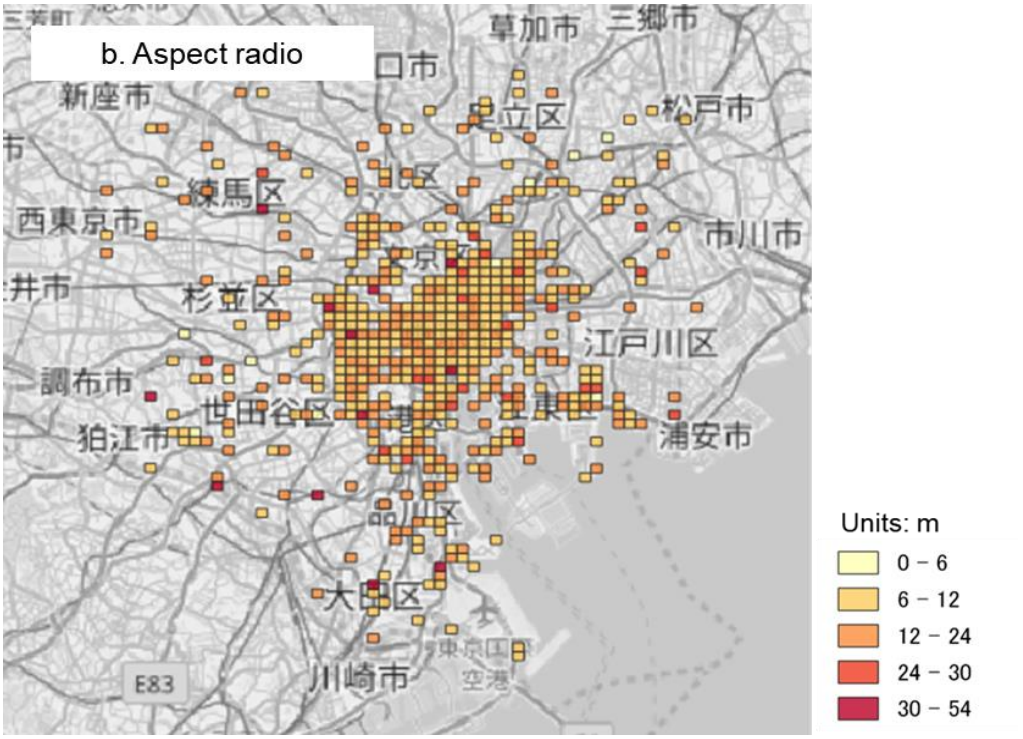
b. Aspect radio
草加市
三郷市
新座市
足立区
松戸市
練馬区
西東京市
市川市
杉並区
江戸川区
調布市
世田谷区
浦安市
狛江市
品川区
大田区
川崎市
E83
空港
Units: m
0 – 6
6 – 12
12 – 24
24 – 30
30 – 54

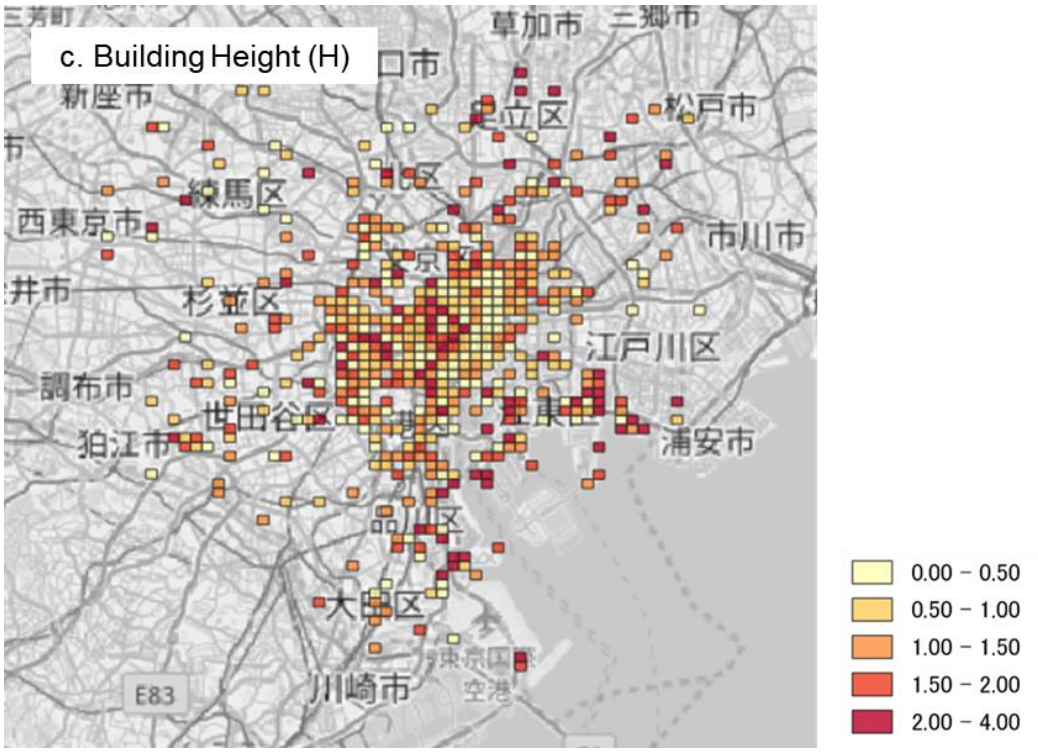

Figure 5.7. Distribution of morphological parameters. (only office and commercial building blocks was showed). (a) Building coverage; (b) Aspect radio; (c) H

5.3.2 Correlation analysis

In the previous part, the correlation between urban geometry parameters and MRT drop was analyzed visually through their distribution on the grids map. In this part, building coverage, aspect ratio and average building height were tested for the correlation with the MRT drop at 15:00 by means of regression analysis, respectively.

The analysis results were showed in Figure 5.8. In the figure, the MRT drop increased with the increase of building coverage, presenting a strong positive correlation with a R square value of 0.799. distribution. And the positive correlation could also be found between the aspect ratio and MRT drop, with a R square of 0.623. It is because the proportion of road areas reduces as the value of building coverage and aspect ratio become larger, resulting in the reduction of solar radiation which is reflected upward to the sky per unit area. For the average building height, it was negatively correlated with MRT drop. It is due to the reduction of solar radiation incident on the lower window surface caused by the shading effect between buildings.

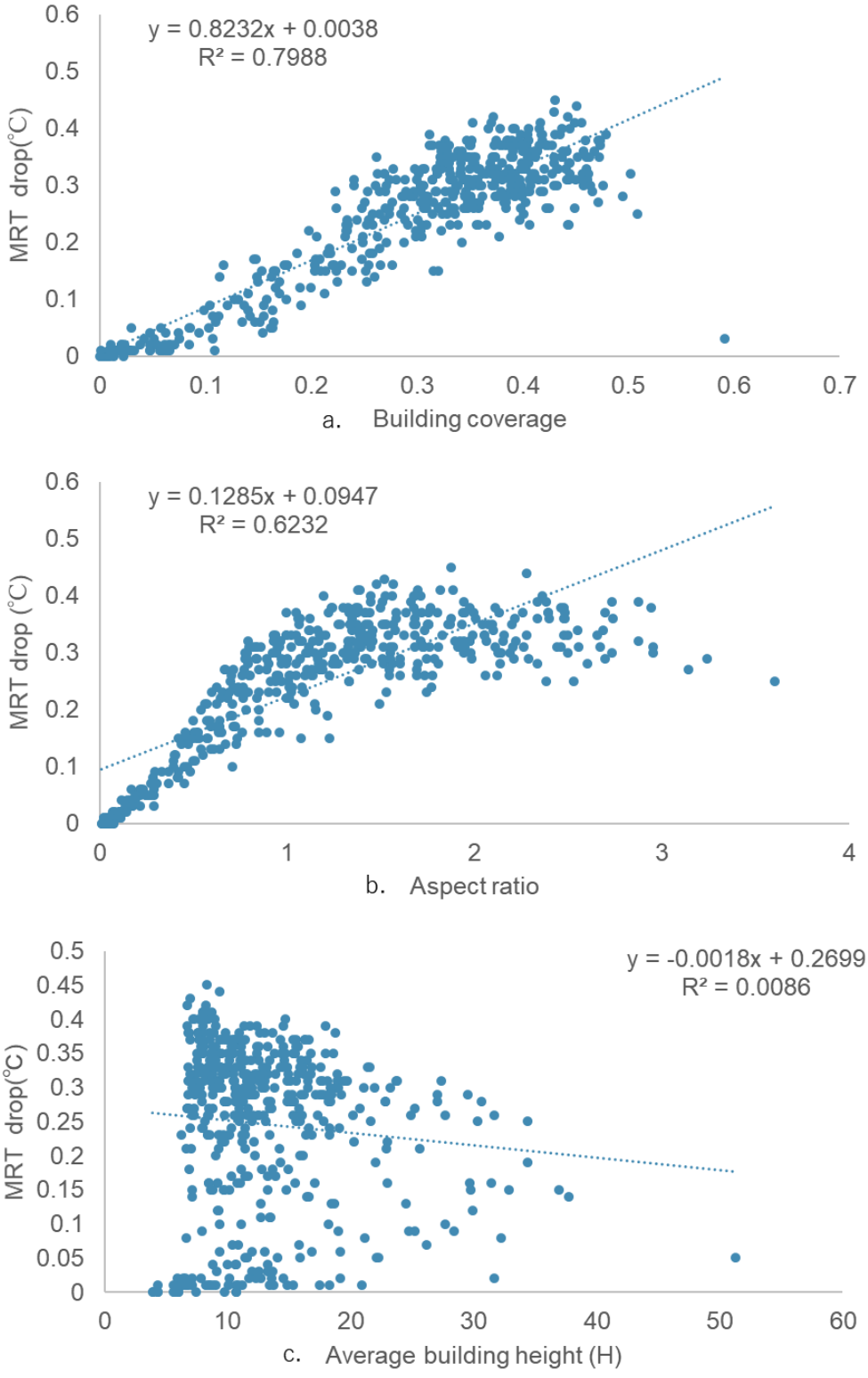

Figure 5.8. Correlation between shape parameters and MRT drop at 15:00

5.3.3 Prediction model

The prediction models of the MRT drop at 12:00, 14:00 and 15:00 were established respectively, taking the building coverage (BC) and average building height (H) as variables. To avoid high correlations between variables, aspect ratio in which the H is involved was not considered in the model.

As showed in Table 5.1, 5.2 and 5.3, all the results are statistically meaningful with a p-value is equal to 0. The values of MRT drop were positively correlated with building coverage and negatively correlated with building height. The coefficient of building coverage is larger than that of building height, which means the building coverage are more important than building height for the prediction of MRT drop. Table 5.4 shows the summary of regression analysis. It can be found that there is a difference among the prediction accuracy of MRT drop at different times. The R square was maximum for MRT drop at 15:00 and minimum at 12:00. As known in the beginning of this chapter, the MRT drop at 12:00, 14:00 and 15:00 increased successively. In other words, the value of MRT drop can be predicted more accurately though geometry parameters BC and H as the value increases. It is because at 12:00 on a summer day, the sun rises to the highest location, the influence of shading effect on the direct solar radiation incident on the building walls becomes less. That is, even the geometry parameters are greatly different, the amount of solar radiation gains of the windows surfaces in each block are almost the same. For this reason, the reduction effect of RRF on MRT depends more on the retro reflectance of windows than the amount of incident direct solar radiation.

Table 5.1. Coefficients of H and BC for MRT drop at 12:00

	Coefficients (95% confidence intervals)	Standard Error	t-value	P-value
H	-0.0010(-0.0013, -0.0007)	0.00015	-6.58	0.00
BC	0.1806(0.1666, 0.1947)	0.007	25.24	0.00

Table 5.2. Coefficients of H and BC for MRT drop at 14:00

	Coefficients (95% confidence intervals)	Standard Error	t-value	P-value
H	-0.0009(-0.0015, -0.0003)	0.0003	-2.92	0.00
BC	0.6100(0.5818, 0.6381)	0.014	42.60	0.00

Table 5.3. Coefficients of H and BC for MRT drop at 15:00

	Coefficients (95% confidence intervals)	Standard Error	t-value	P-value
H	-0.00225(-0.0030, -0.0015)	0.0004	-5.76	0.00
BC	0.82564(0.7899, 0.8613)	0.018	45.48	0.00

Table 5.4. Summary statistics of regression analysis for the MRT drop at 12:00, 14:00 and 15:00

	12:00	14:00	15:00
Multiple R	0.76	0.89	0.90
R square	0.58	0.78	0.81
Adjusted R square	0.57	0.78	0.81
Standard Error	0.02	0.04	0.05
Observations	465	465	465

5.4 Mitigation of the heat illness risk

Wet Bulb Globe Temperature (WBGT) has been specified as a heat illness risk on the Japanese Ministry of the Environment's heat illness prevention website since 2006.It is more likely to suffer from heat-related illness in the environment with high temperature, high humidity and lack of shade. Figure 5.9 shows the variation of daily occurrence of heat illness with the maximum WBGT. In the figure, the cases of heat illness increase dramatically when the maximum WBGT exceeds 28℃. The heat illness risk is divided into four grades (danger, sever warning, warning and caution) according to maximum WBGT as showed in Table 5.5.

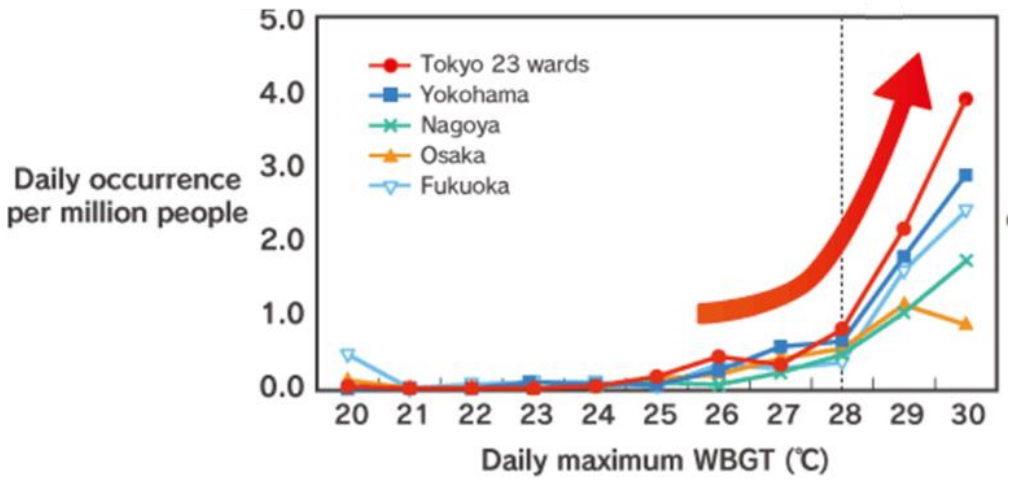

Fig 5.9. Variations of daily occurrence of heat illness with the maximum WBGT in the major cities in Japan. (Ministry of the Environment Government of Japan, 2019)

Table 5.5. Heat illness risk grades based on the maximum WBGT. (Ministry of the Environment Government of Japan, 2019)

WBGT range	Heat illness risk grades
≥ 31 ℃	Danger (danger in all life activities)
28 - 31 ℃	Severe Warning (danger in all life activities)
25 - 28 ℃	Warning（danger in moderate life activities）
< 25 ℃	Caution（danger in vigorous-intensity life activities）

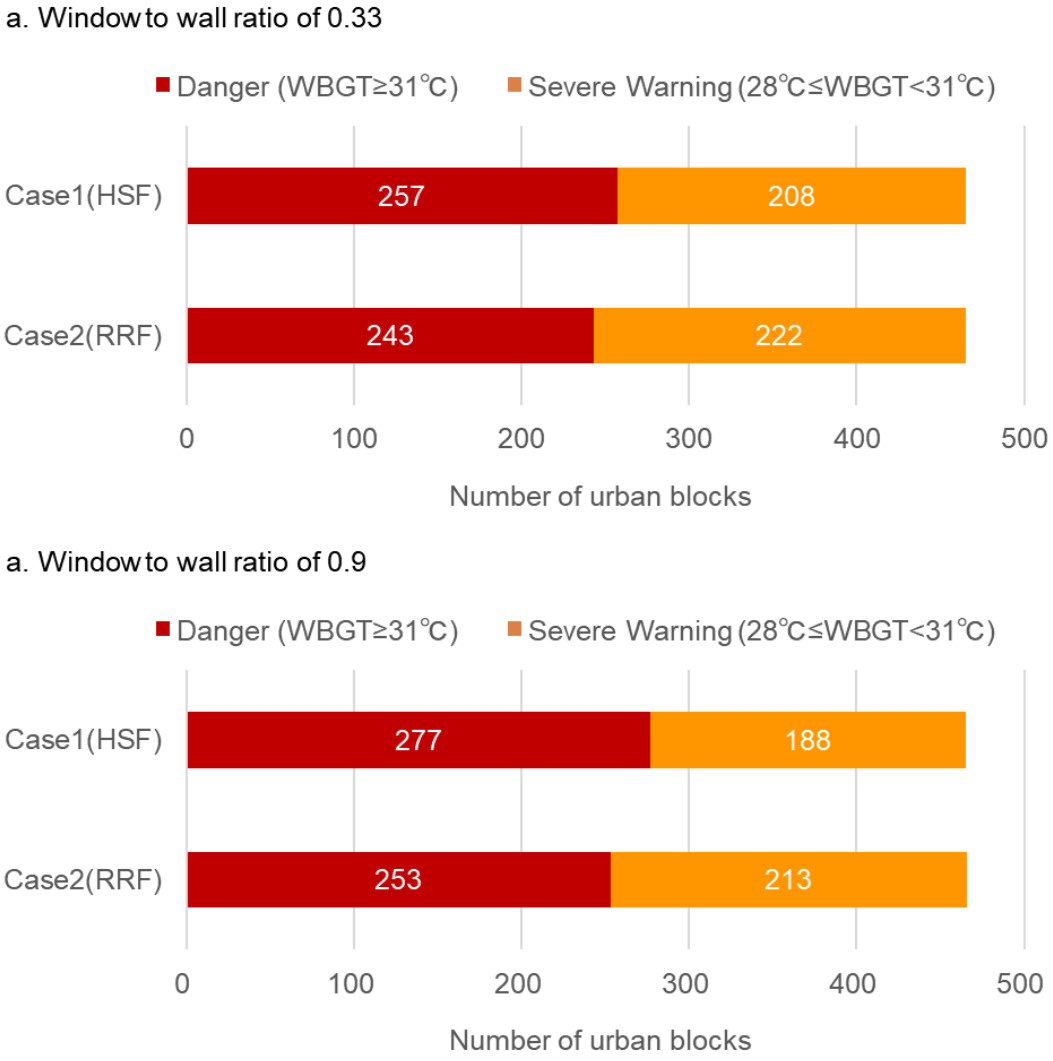

Figure 5.10. Number of office and commercial building blocks with different heat illness risk grades determined by maximum WBGT on a sunny day (August 5, 2006)

Figure 5.10 shows the number of blocks with different heat illness risk grades on a sunny day. The maximum WBGT in all office and commercial building blocks exceeded 28 ℃, indicating a high risk of heat-related illness. For the block with window to wall ratio of 0.33, the number of blocks where the maximum WBGT exceeds 31℃ heat illness risk grade of "danger") was 257 in Case1 (HSF) while that number was 243 in Case2 (RRF). Compared with HSF, the installation of RRF reduced the number of blocks with heat illness risk grade of "danger" decreased by 14. For the block which has a window ratio of 0.9, the number of blocks with the maximum WBGT above 35℃ was 277 in Case1 (HSF) and 253 in Case2 (RRF), reducing by 24.

The number of office and commercial building blocks with heat illness risk grade of “danger” decreased as a result of the installation of RRF. The higher the window-wall ratio, the more the number of blocks being reduced. However, the number of these “danger” blocks also increased with the increase of window areas. The degradation of outdoor thermal comfort was caused by the increase in the total amount of the solar radiation downward reflected by the window.

5.5 Conclusion

To sum up, for the time variation of effects, the value of average Δ MRT (HSF-RRF) maximized at 9:00 (0.29℃) and 15:00 (0.26℃), while it became not obvious at approximately noon when the outdoor radiant environment was worst. However, the value of Δ MRT (HSF-RRF) increased during the time period of 14:00 and 16:00 when the outdoor thermal comfort was still at a low level with a high value of WBGT. For the geographical distribution of Δ MRT (HSF-RRF), the values are larger in the central business areas. By comparing with the heat disorder risk map of Tokyo 23 wards (Ohashi et al, 2016), those areas with the high heat disorder risk also have larger value of Δ MRT (HSF-RRF).

Subsequently, the relationship between the Δ MRT (HSF-RRF) and urban geometry parameters was explored through the linear regression analysis and a strong positive correlation ($R^2 = 0.8$) was found between building coverage (BC) and Δ MRT (HSF-RRF).

What's more, the effects on the heat illness risk which is determined by maximum WBGT were also evaluated in this work. Due to the installation of RRF, the number of "danger" blocks ($\mathrm{WBGT}_{max} > 35$℃) reduced by 14 and 24 in the case with WWR of 0.33 and 0.9 respectively. It is indicated that RRF can mitigate the heat illness risk in outdoor spaces to some extent.

CHAPTER 6. EFFECTS ON THE COOLING ENERGY CONSUMPTION

6.1 Simulation conditions

6.1.1 Simulation cases

The Simulation was conducted in the three office blocks with different values of building coverage. As showed in Figure 6.1, the simulated blocks are all located in the central business district in Tokyo. Their geometry parameters were listed Table 6.1. In order to evaluate the impact of building coverage (BC) on the cooling energy consumption with the less interference, the blocks with almost the same building height and located in the center of Tokyo. were selected intentionally.

The single-float glass (SFG), heat shading (HSF) and retro-reflective (RRF) window, which were also used in the previous analysis, were installed in each block. In addition, considering the increase of newly built buildings constructed by glass curtain wall in the center business district, the cases with the window to wall ratio (WWR) of 0.9 were also analyzed.

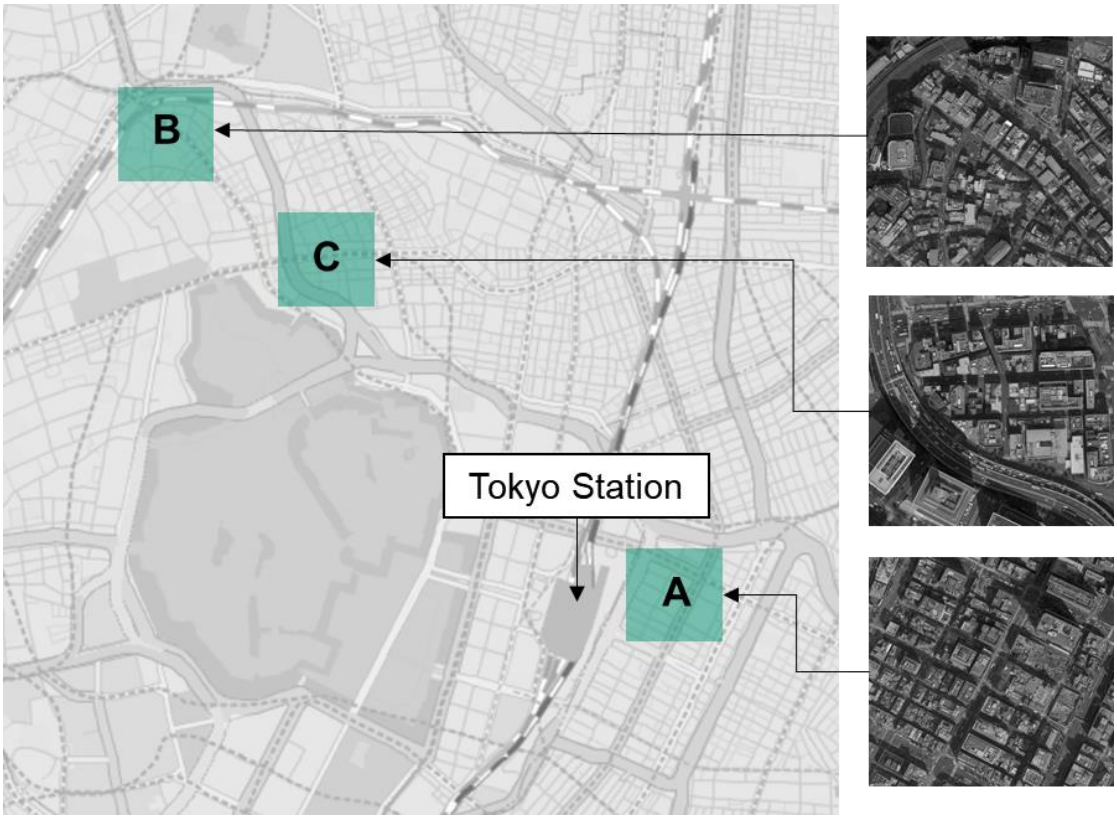

Figure 6.1. Locations of simulated blocks and their satellite images

Table 6.1. Geometry parameters of simulated blocks.

	Building width (m)	Building height (m)	Road width (m)	Building coverage (BC)
A block	17.61	25.19	8.02	0.47
B block	16.55	23.77	12.22	0.33
C block	18.19	23.00	22.76	0.19

6.1.2 Building structures

For the structures of the buildings, the parameters of typical office buildings were adopted for the materials of building envelop as shown in Table 6.2. The exterior concrete walls and walls were set to 22cm and 21cm in thickness, respectively and expressed by equally divided 16 layers. The window to wall ratio was set to 0.33.

Table 6.2. Parameters of the building envelop materials used in the calculation

	Surface albedo	Volumetric heat capacity ($Jm^{-3}\,K^{-1}$)	Thermal conductivity($Wm^{-1}\,K^{-1}$)
Wall materials	0.2	1725964	0.6
Roof materials	0.2	1839556	0.3

For air conditioning in the buildings, the typical conditions for office buildings were also adopted as shown in Table 6.3 and Table 6.4. Considering the heat source composition in the cooling system that was installed in this block, it was assumed that 47% of the heat-source equipment was town gas driven and the remaining 30% was the electric air-source heat pump.

Table 6.3. Parameters of the air conditioning (Central Research Institute of Electric Power Industry, 1998)

Parameters	settings
Target temperature (℃)	26
Ratio of air-conditioning floor area to total floor area (℃)	0.7
Duration of air-conditioning on weekdays	Table. 7.3
Occupancy rate ($person\ m^{-2}$)	Table. 7.3

Ventilation frequency(time h^{-1})	0.5
Sensible heat generation from an occupant ($Jm^{-3}\,K^{-1}$)	59
Latent heat generation from an occupant ($Jm^{-3}\,K^{-1}$)	31

Table 6.4. Parameters of the air conditioning operating schedule (Agency for Natural Resources and Energy, 2011)

Time	Air conditioning operation rate (–) [15]	Occupancy rate (person m^{-2}) [16]
1	0.14855381	0
2	0.136942419	0
3	0.133880159	0
4	0.134819434	0
5	0.133404167	0
6	0.141034329	0
7	0.157511984	0
8	0.185522052	0
9	0.216704335	0.1
10	0.246559726	0.75
11	0.273344894	0.75
12	0.292576969	0.75
13	0.303609905	0.3
14	0.309851334	0.75
15	0.309639611	0.75
16	0.313118644	0.75
17	0.320739091	0.75
18	0.320663795	0.3
19	0.305782446	0.3
20	0.275718613	0.3
21	0.247304615	0
22	0.2215986	0
23	0.196031979	0
24	0.169750736	0

6.2 Results

Table 6.5 shows the total amount of cooling energy consumption in August in each case. The maximum amount of cooling energy consumption was 19.37 kWh/m^2 in the case of (BC=0.19, WWR=0.9, SFG) and minimum amount was 15.37 kWh/m^2 in the case of (BC=0.47, WWR=0.33, RRF). By comparing the cooling energy consumption in the cases with different BC, it can be found that for all windows, the consumption amount increased with the increase of BC due to the reduction of heat entering the room, which is caused by the shading effect between buildings. And the cooling energy consumption in the case with WWR of 0.9 was greater than that in the cases with WWR of 0.33 owing to the increase of the transmission of the solar insolation through the windows.

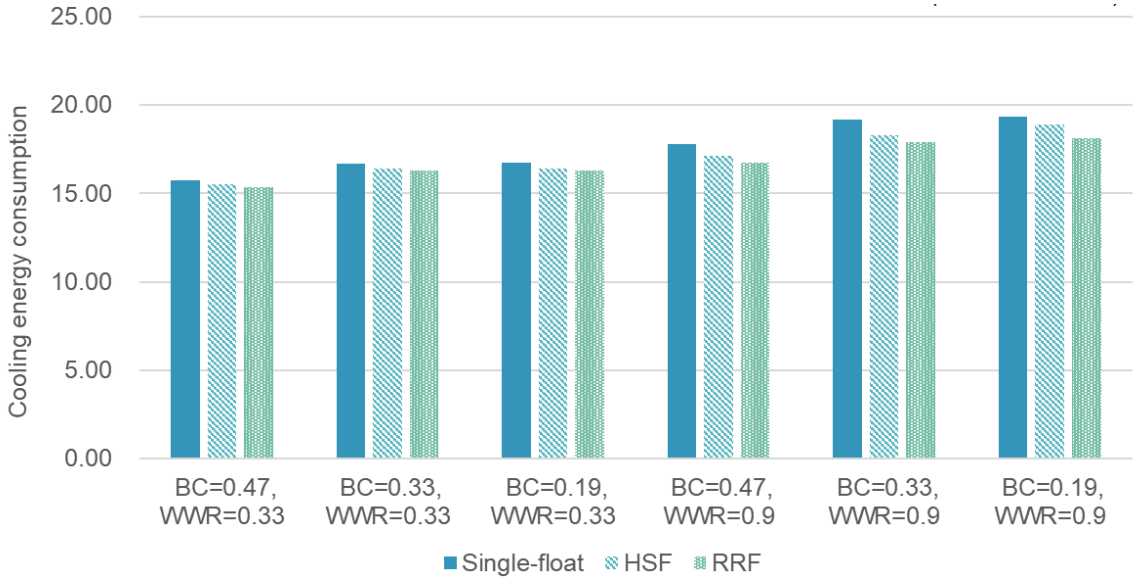

Figure 6.2 Comparisons of total cooling energy consumption in August (kWh/m^2)

Table 6.5 Total amount of cooling energy consumption in August in each case (kWh/m^2)

	SFG	HSF	RRF
BC=0.47, WWR=0.33	15.74	15.49	15.37
BC=0.33, WWR=0.33	16.70	16.41	16.28
BC=0.19, WWR=0.33	16.72	16.41	16.28
BC=0.47, WWR=0.9	17.82	17.12	16.74
BC=0.33, WWR=0.9	19.16	18.30	17.88
BC=0.19, WWR=0.9	19.37	18.92	18.10

Table 6.6 shows the comparison of cooling energy consumption between SFG, HSF and RRF. In all blocks, the installation of both HSF and RRF reduced the cooling energy consumption and the reduction effects of RRF was larger than that of HSF, with the maximum amount of 1.28 kWh/m^2 (6.7%) in the case of (BC=0.33, WWR=0.9). It is because the transmittance of SFG, HSF and RRF decreased sequentially as shown in Table 3.4. Compared with HSF, the cooling energy consumption of RRF decreased largest by 0.82 kWh/m^2 (4.3%) in the case of (BC=0.19, WWR=0.9).For the cases with different BC, the value of Δ (RRF-HSF) increased as the BC decreases. It is for the reason that the more the solar radiation incident on the window surface, the more the amount of that being blocked out, due to the lower transmittance of RRF compared with the HSF.

However, for the value of Δ (RRF-SFG) and Δ (HSF-SFG) in the cases with WWR of 0.9, the maximum value happened in the block where the BC is equal to 0.33 rather than 0.19. It is because the solar radiation incident on the window concludes not only the direct solar radiation (hereinafter referred to as "D") but also the reflected solar radiation from the opposite windows (hereinafter referred to as "R"). The closer the distance between buildings, the greater the amount of D. Thus, with the increase of BC, although the amount of R decreases, the amount of D increased. In the cases with low WWR, the increase in that D is not significant, so the values of Δ (RRF-SFG) and Δ (HSF-SFG) in the case (BC=0.19) are still the largest. However, as the WWR increases, it become larger, which make the amount of blocked radiation by RRF and HSF increases and finally results in that the values of Δ (RRF-SFG) and Δ (HSF-SFG) in the case (BC=0.33) exceeds that in in the case (BC=0.19). However, the same phenomenon did not appear in the value of Δ (RRF-HSF).

Table 6.6. Comparison of cooling energy consumption in August between SFG, HSF and RRF in different blocks (Unit: kWh/m^2)

	Δ (HSF−SFG)	Δ (RRF−SFG)	Δ (RRF−HSF)
BC=0.47, WWR=0.33	-0.24 (-1.5%)	-0.37 (-2.3%)	-0.12 (-0.79%)
BC=0.33, WWR=0.33	-0.29 (-1.7%)	-0.42 (-2.5%)	-0.13 (-0.82%)
BC=0.19, WWR=0.33	-0.30 (-1.8%)	-0.44 (-2.6%)	-0.14 (-0.83%)
BC=0.47, WWR=0.9	-0.70 (-3.9%)	-1.07 (-6.1%)	-0.38 (-2.2%)
BC=0.33, WWR=0.9	-0.86 (-4.5%)	-1.28 (-6.7%)	-0.42 (-2.3%)
BC=0.19, WWR=0.9	-0.44 (-2.3%)	-1.26 (-6.5%)	-0.82 (-4.3%)

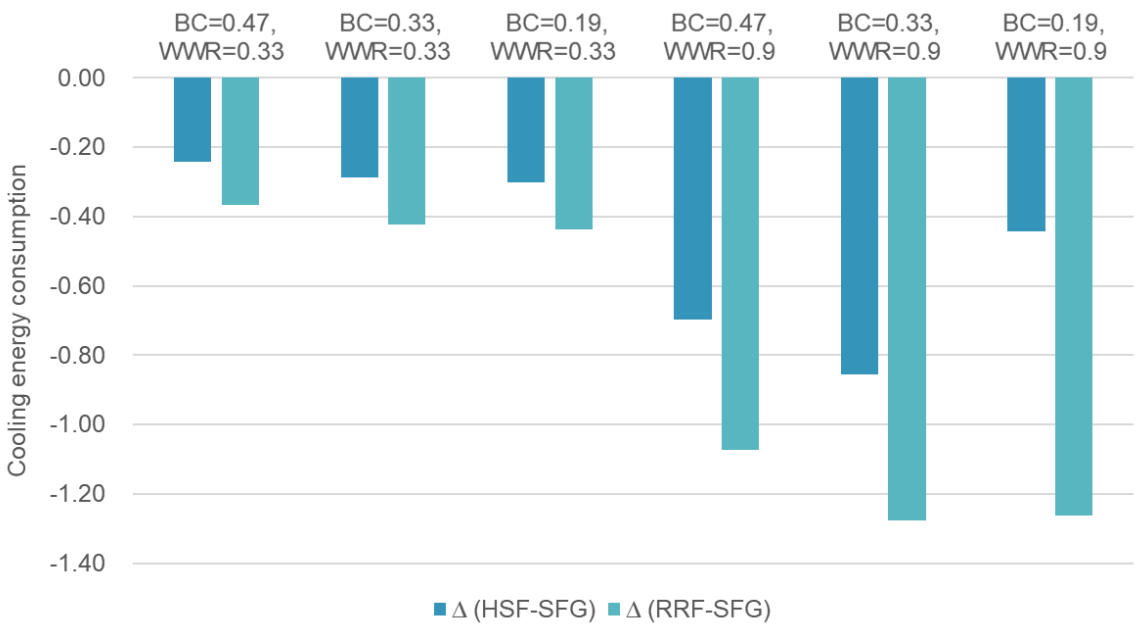

Figure 6.3 Comparisons of Δ (HSF−SFG) and Δ (RRF−SFG) (Unit: kWh/m^2)

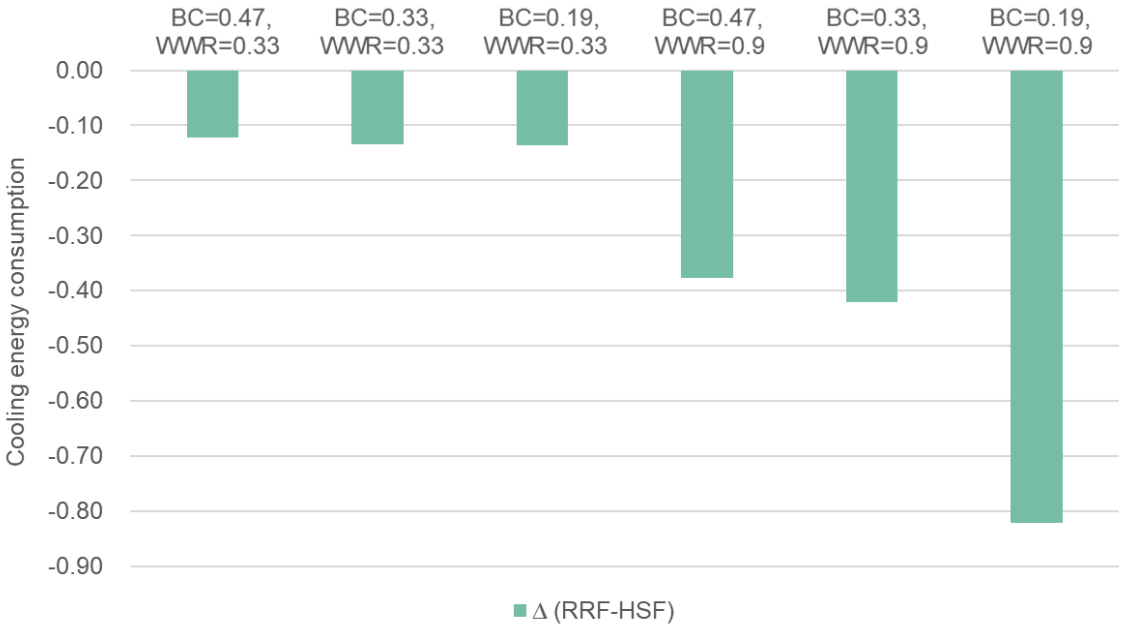

Figure 6.4 Comparisons of Δ (RRF−HSF) (Unit: kWh/m^2)

6.3 Conclusions

To sum up, the installation of both RRF and HSF can reduce the energy consumption of air-conditioning in summer days and RRF could further reduce it compared with HSF. For all types of windows, the cooling energy consumption increase with the increase of window to wall ratio (WWR) and the reduction of building coverage (BC). The impacts of BC on the energy-saving effects of RRF and HSF are different between the low WWR and high WWR. Moreover, compared with HSF, the energy-saving effects of RRF are more significant in the areas with low density where the more cooling energy demand is needed.

7. Conclusion

In this study, to assess feasibility of the large-scale application of RRF to the exterior wall of buildings in actual urban areas, the effects of RRF both on the outdoor thermal environment in summer and cooling energy consumption was evaluated in the business district of Tokyo 23 wards, using the CM-BEM model coupled with a new developed computational model of radiation heat transfer considering the specular and retro reflections of solar radiation

In Chapter 2, the basic framework and computational flow of simulation systems (WRF-CM-BEM) was introduced, followed by the fundamental equations for the dramatic calculation of the atmospheric temperature in the CM and the cooling energy consumption in BEM, as well as the calculation of thermal indices. Next, the new developed computational method of radiative heat transfer considering the specular and retro reflection of solar radiation was described in Chapter 3. With the consideration of directional reflection from window surface, the proportion of the reflected solar radiation from window surface to ground or wall surface become time-dependent (while it is a constant value for diffuse reflection) and its value was calculated by analytic geometry. In addition, the Angular-dependent optical properties were also considered and obtained with empirical formulas.

In Chapter 4, the proposed method was validated by comparing with the simulated results obtained with CFD model (Yoshida and Moshida, 2017; Yoshida et al, 2018). Then, it was applied to evaluate the impact of RRF on the outdoor thermal environment in summer (Chapter 5) and cooling energy consumption (Chapter 6).

For the effects on the outdoor thermal environment, the value of average ΔMRT (HSF-RRF) maximized at 9:00 (0.29℃) and 15:00 (0.26℃), while it became not obvious at approximately noon when the outdoor thermal environment is worse. However, the value of Δ MRT (HSF-RRF) increased during the time period of 14:00 and 16:00 when the outdoor thermal comfort was still at a low level with a high value of WBGT. For the geographical distribution of Δ MRT (HSF-RRF), the values are larger in the central business areas near Tokyo station. By comparing with the heat disorder risk map of Tokyo 23 wards (Ohashi et al, 2016), those areas with the high heat disorder risk also have larger value of ΔMRT (HSF-RRF). Subsequently, the relationship between the ΔMRT (HSF-RRF) and urban geometry parameters was explored through the linear regression analysis and a strong positive correlation ($R^2 = 0.8$) was found between building coverage (BC) and ΔMRT (HSF-RRF).What's more, the effects on the heat illness risk which is determined by maximum WBGT were also evaluated in this work. Due to the installation of RRF, the number of "danger" blocks ($WBGT_{max}$>35℃) reduced by 14 and 24 in the case with WWR of 0.33 and 0.9, respectively. It is indicated that RRF can mitigate the heat illness risk in outdoor spaces to some extent.

For the effects on the cooling energy consumption, the energy-saving effects was found in both HSF and RRF. And compared with HSF, RRF can further reduce the energy consumption. Moreover, the reduction effects increased as the BC decreases. It is indicated that energy-saving effect of RRF is more significant where the more energy demand is needed with a low density and high WWR)

To sum up, it is revealed that the improvement effects of RRF on the outdoor thermal environment become larger in the high-density areas with a worse thermal environment, and the energy-saving effects increase in the low-density areas where more cooling energy is consumed. And the mitigation effects of RRF on outdoor heat illness risk could also be observed in the business district with a high density of population in Tokyo 23 wards.

Future work

Since the retro-reflective film may cause the opposite effects in winter, the annual evaluation should be addressed. As the heat illness risk varies differently in the sun and shade areas of the street, the distribution of improvement effects on the thermal environment in street spaces should be evaluated in the future. Moreover, as another important influence factor on urban thermal environment, the impact of urban orientation on the performance of retro-reflective film also need to be assessed in the future.

References

(Bueno B et al, 2012) Bueno B, Norford L, Pigeon G, Britter R. (2018). A resistance capacitance network model for the analysis of the interactions between the energy performance of buildings and the urban climate. Build Environ, 54, 116–25.

(Harima and Nagahama, 2017b) h. Harima T, Nagahama T (2017b). Evaluation methods for retroreflectors and quantitative analysis of near infrared upward reflective solar control window film—Part II: Optical properties evaluation and verification results. Solar Energy, 148, 164–176.

(Kondo and Liu, 1998) Kondo H, Liu H. (1998). A study on the urban thermal environment obtained through one-dimensional canopy model. Journal of Japan Society for Atmospheric Environment, 33(3), 179–92.

(Kikegawa et al, 2003) Kikegawa Y, Genchi Y, Yoshikado H, & Kondo H. (2003). Development of a numerical simulation system toward comprehensive assessments of urban warming countermeasures including their impacts upon the urban buildings' energy-demands. Applied Energy, 76(4), 449-466.

(Kim et al, 2009) Kim J, Ito H, Tanabe S. (2009). The thermal performance by future forecast model of glass façade buildings. Journal of Environmental Engineering, 74(646), 1283-1289

(Lai et al, 2019) Jamei E, Rajagopalan P, Seyedmahmoudian M and Jamei Y. (2016). Review on the impact of urban geometry and pedestrian level greening on outdoor thermal comfort, Renewable and Sustainable Energy Reviews, 54, 1002-1017.

(Makino, 1999) Makino T, Nakamura A, Wakabayashi H (1999). Directional characteristics of radiation reflection on rough metal surfaces with description of heat transfer parameters. The Japan Society of Mechanical Engineering, 65(630), 324–330. (in Japanese with English abstract)

(Nakaohkubo et al, 2008) Nakaohkubo K, Hoyano A, Asawa T, Fukasawa H. (2008) Development of outdoor heat balance simulation considering directional characteristics of reflected solar radiation from the building external surfaces, Journal of Environmental Engineering, 73(625), 275-282 (in Japanese with English abstract)

(Ohashi et al, 2014) Y. Ohashi, Y. Kikegawa, T. Ihara, N. Sugiyama. (2014). Numerical simulations of outdoor heat stress index and heat disorder risk in the 23 wards of Tokyo, J.Appl. Meteor. Climatol. 53 (3), 583–597.

(Ohashi et al, 2016) Ohashi Y, Ihara T, Kikegawa Y, Sugiyama N. (2016). Numerical simulations of influence of heat island countermeasures on outdoor human heat stress in the 23 wards of Tokyo, Japan Energy and Buildings, 114, 104–111

(Sakai et al, 2011) Sakai S, Iyota H, Emura K, Igawa N. (2011). Development and evaluation of directional retroreflective materials as a heat island countermeasure Part 1. Journal of Structural and Construction Engineering, 76 (665), 1229–1234.

(Siegel and Howell, 2001) Siegel R, Howell J, Thermal Radiation Heat Transfer. CRC Press, 2001

(Sailor DJ,2011) Sailor DJ. (2011) A review of methods for estimating anthropogenic heat and moisture emissions in the urban environment. Int J Climatol, 31,189–99

(Santamouris M et al, 2001) Santamouris M, Papanikolaou N, Livada I, Koronakis I, Georgakis C, Argiriou A. (2001). On the impact of urban climate to the energy consumption of buildings. Sol Energy, 70(3), 201–16.

(Taleghani M et al, 2014) Taleghani M, Tenpierik M, van den Dobbelsteen A, Sailor DJ. (2014). Heat in courtyards: avalidated and calibrated parametric study of heat mitigation strategies for urban courtyards in the Netherlands. Sol Energy, 103, 108–24.

(Taleghani M et al, 2015) Taleghani M, Kleerekoper L, Tenpierik M, van den Dobbelsteen A. (2015). Outdoor thermal comfort within five different urban forms in the Netherlands. Build Environ, 83, 65–78.

(Taleghani M et al, 2013) Taleghani M, Tenpierik M, Kurvers S, Dobbelsteen A. (2013). A review into thermal comfort in buildings. Renew Sustain Energy Rev, 26(0), 201–15.

(Yoshida and Moshida, 2017) (2017) Evaluation on effects of heat ray retro reflective film using a CFD analysis coupled with radiant computation considering directional reflection (Part 4) Effects of considering directional reflection of solar radiation on thermal comfort for pedestrians in summer season. The Society of Heating, Air-Conditioning and Sanitary Engineers of Japan (CD-ROM), F-59, p.ROMBUNNO. F-59. (in Japanese)

(Yoshida et al, 2018) Yoshida S, Mochida A. (2018). Evaluation of effects of windows installed with near-infrared ray retro-reflective film on thermal environment in outdoor spaces using CFD analysis coupled with radiant computation, Building Simulation, 11, 1053–1066.

(Siegel and Howell, 2001) Siegel R, Howell J, Thermal Radiation Heat Transfer. CRC Press, 2001

(Agency for Natural Resources and Energy, 2011) 資源エネルギー庁. 夏期最大電力使用日の需要構造推計（東京電力管内）
<http://www.meti.go.jp/setsuden/20110513taisaku/16.pdf>

Central Research Institute of Electric Power Industry, 1998) 事務所ビルの省エネルギー−東京都区部における可能量と必要コストの評価

(Dexerials Corporation HP, 2019) 製品情報：熱線再帰フィルム <https://www.dexerials.jp/en/products/d1/iravk700.html>

(Japan Meteorological Agency) 気象庁ホームページ掲載されたデータより作成 <https://www.jma.go.jp/jma/menu/menureport.html>

(Japan Meteorological Agency, 2013) ヒートアイランド現象の要因について <http://www.data.jma.go.jp/cpdinfo/himr_faq/02/qa.html>

(Ministry of the Environment Government of Japan, 2013) ヒートアイランド現象に対する適応策及び震災後におけるヒートアイランド対策検討調査業務報告書

(Ministry of the Environment Government of Japan, 2019) 熱中症予防情報サイト <http://www.wbgt.env.go.jp/>

(Tokyo, 2013) 平成 23 年度区部土地利用現況調査

(Tokyo Environment Bureau, 2005) ヒートアイランド対策ガイドライン <http://www.kankyo.metro.tokyo.jp/climate/heat_island/guideline.files/heatguideline.pdf>